Twilight Near-Infrared Radiometry for Stratospheric Aerosol Layer Height

Lipi Mukherjee[1,2], Dong L. Wu[2], Nader Abuhassan[1,3,4], Thomas F. Hanisco[3], Ukkyo Jeong[5], Yoshitaka Jin[6], Thierry Leblanc[7], J. Ben Liley[8], Bernhard Mayer[9], Forrest M. Mims III[10], Isamu Morino[6], Tomohiro Nagai[11], Peter Pantina[12,2], Richard Querel[8], Tetsu Sakai[11], Osamu Uchino[11], Ellsworth J. Welton[13], and Stephen Windle[14]

[1]GESTAR-II/University of Maryland Baltimore County
[2]Climate and Radiation Lab, NASA Goddard Space Flight Center
[3]Atmospheric Chemistry and Dynamics Laboratory, NASA Goddard Space Flight Center
[4]Sciglob Instrument and Services,9881 Broken Land Pkwy, Columbia, MD 21046
[5]Pukyong National University, Busan, Republic of Korea 48513
[6]National Institute for Environmental Studies, 16-2 Onogawa, Tsukuba, Ibaraki 305-8506, Japan
[7]Jet Propulsion Laboratory, California Institute of Technology, Wrightwood, CA 92397, USA
[8]National Institute of Water & Atmospheric Research Ltd (NIWA), Lauder, New Zealand
[9] Lehrstuhl fuer Experimentelle Meteorologie Ludwig-Maximilians-Universitaet Theresienstrasse 37, 80333 Muenchen
[10]Geronimo Creek Atmospheric Monitoring Station
[11]Meteorological Research Institute, Japan Meteorological Agency, 1-1 Nagamine, Tsukuba, Ibaraki, 305-0052, Japan
[12]Science Systems and Applications, Inc. (SSAI)
[13]Mesoscale Atmospheric Processes, NASA Goddard Space Flight Center
[14]Department of Atmospheric and Oceanic Science, University of Maryland, College Park, MD, USA

1 Abstract

The impact of stratospheric aerosols on Earth's climate, particularly through atmospheric heating and ozone depletion, remains a critical area of atmospheric research. While satellite data provides valuable insights, independent validation methods are necessary for ensuring accuracy. Twilight near-infrared (NIR) radiometry offers a promising approach for investigating aerosol properties, such as optical depth and layer height, at high altitudes. This study aims to evaluate the effectiveness of twilight radiometry in corroborating satellite data and assessing aerosol characteristics. Two methods based on twilight radiometry—the color ratio and the derivative method—are employed to derive the aerosol layer height and optical depth. Radiances at 450, 550, 762, 775, and 1050 nm wavelengths are analyzed at varying solar zenith angles, using zenith viewing geometry for consistency. Comparisons of aerosol optical depths (AODs) between Research Pandora (ResPan) and AErosol RObotic NETwork (AERONET) data (R = 0.99) and between ResPan and Modern-Era Retrospective analysis for Research and Applications (MERRA-2) data (R = 0.86) demonstrate a strong correlation. Twilight ResPan data are also used to estimate the aerosol layer height, with results in good agreement with SAGE and lidar measurements, particularly following the Hunga Tonga eruption in Lauder, New Zealand. The simulation database, created using the libRadtran DISORT and Monte Carlo packages for daylight and twilight calculations, is capable of detecting AODs as low as 10^{-3} using the derivative method. This work highlights the potential of twilight radiometry as a simple, cost-effective tool for atmospheric research and satellite data validation, offering valuable insights into aerosol dynamics at stratospheric altitudes.

2 Introduction

Twilight influences life on Earth, with its illumination varying by latitude and season due to the atmospheric density [1]. It affects plant growth and blooming times, while also providing cooler temperatures and favorable hunting conditions for wildlife. The low light conditions during this transitional period with fish coming to the surface of the water to nourish themselves before going back to deeper waters, [2, 3], make it an ideal time for fishing activities. As such, twilight plays a critical role in the ecosystems of many regions, influencing both natural processes and human activities.

Twilight can be classified into three distinct phases, each marked by a specific angle of solar depression below the horizon [4]. Civil twilight, when the Sun is between $0°$ and $6°$ below the horizon, is good for landscape imaging. Next is nautical twilight when the Sun is between $6°$ and $12°$ below the horizon. During this time some major stars are visible which help the sailors in navigation. The last is astronomical twilight, when the geometric center of the Sun is between $12°$ and $18°$. Astronomers use the astronomical twilight time to observe stars or planets that appear as bright points. It should be noted that the illumination level of different twilight periods depends not only on the depression of the Sun but also on the presence of clouds.

Twilight sky brightness is caused by sunlight scattered by molecules, aerosols, and ozone in a thin volume of air above the momentary height of Earth's shadow during sunset/sunrise, as shown in Figure 1. This phenomenon is measured through twilight radiometry (TRM), a technique that has been employed since the early 19th century to study the vertical optical properties of the atmosphere. In an attempt to record daylight illumination, the study was extended to the Sun's depression angles of 2°, 3°, and 6°, respectively, using a visual photometer [5, 6]. Subsequently, the shortening of civil twilight in the presence of clouds was investigated [6]. An increase in twilight sky brightness due to forest fires was also observed [6]. The measurements were made using a Weber photometer with the Sun at a depression of 8°. A wedge photometer measured twilight intensity at Sun depression angles of 8.5° to 13.5°, establishing the relationship between decreasing intensity and increasing solar depression [6].

Despite these foundational studies, several critical gaps in the understanding of twilight brightness remained unresolved. One significant challenge was the difficulty in comparing twilight measurements across different observers, due to inconsistent methodologies and a lack of standardized absolute twilight intensity data. As a result, the connection between twilight brightness and the optical properties of Earth's atmosphere remained understudied. Additionally, the limited range of solar depression angles investigated further constrained the depth of these studies. These issues persisted even as researchers like [6] expanded their observations, using both visual photometers and photoelectric cells and presented data on air density as a function of altitude. These methods were later applied to detect aerosol and dust layers in the atmosphere by measuring variations in twilight intensity [7, 8]. Their work concluded that twilight intensity could be a reliable method for observing dust in the atmosphere. Furthermore, while some research suggested that stratospheric aerosols could influence twilight brightness—particularly after volcanic eruptions [9–13]—there was insufficient observational evidence to quantify this impact reliably. Earlier measurements were often challenged by inconsistent methodologies and limited observational reach for studying stratospheric aerosols.

In addition to these challenges, stratospheric aerosols have been a key focus in Earth science due to their significant impact on climate. These aerosols influence the radiative balance [14], contribute to stratospheric warming, accelerate ozone depletion through chemical reactions, and disrupt global stratospheric dynamics [15]. They are also believed to negatively impact nitrogen dioxide, which plays a crucial role in various stratospheric chemical cycles [16]. Although the stratosphere contains only 17% of the atmosphere's mass, its instability can have a profound influence on the troposphere, which in turn affects surface conditions. Stratospheric aerosols, such as condensed aerosols and mineral dust, can influence climate change both regionally and globally during events of high aerosol injection, such as volcanic eruptions [17].

To improve our understanding of these aerosols, many satellite-borne monitoring instruments are used, providing global-scale data. The Stratospheric Aerosol Measurement (SAM) and later SAM II instruments were developed to analyze stratospheric aerosol data for polar regions. The SAGE missions (SAGE I, II, III) are remote sensing instruments that use the solar occultation technique to study important atmospheric constituents like aerosols, ozone, and water vapor [18–21]. However, the global-scale data provided by these instruments must be validated using other methods, such as in-situ sampling (balloon-borne) and remote scattering measurements like ground-based lidars [22]. Stratospheric aerosols also impact twilight sky brightness. Consequently, measurements of twilight sky brightness caused by aerosol scattering can serve as an alternative method to corroborate satellite-based findings. This serves as the primary motivation for the current study.

The challenges of previous twilight radiometry research are addressed by employing advanced radiative transfer modeling techniques and high-quality observational data. All calculations are performed using the zenith viewing geometry. Compared to direct-Sun geometry, the zenith view provides measurements during twilight and is particularly advantageous for retrieving near-surface species like nitrogen dioxide and formaldehyde [23], especially in thin and moderate cloud conditions when direct Sun measurements are difficult to achieve. Additionally, this viewing geometry can help differentiate between ground surfaces, as will be discussed later. The study of twilight has been conducted using a Monte Carlo-based radiative transfer (RT) model from libRadtran [24], with data obtained from the ResPan spectroradiometer (Reserach Pandora) similar to the one discussed in [25]. The technique is employed to ascertain two key aerosol properties: aerosol optical depth (AOD) and aerosol layer height (ALH). Several key findings are presented in this study.

AOD and ALH are critical parameters for understanding climate dynamics. AOD is an optical parameter of aerosols, widely used as an indicator of air pollution. It reflects how much direct sunlight is blocked by air pollutants (such as dust, smoke, etc.). This dimensionless quantity can impact air quality, climate change, human health, and the balance between incoming solar energy and outgoing radiation from Earth [26]. Knowledge of ALH is essential for determining the impact of aerosols at different vertical heights of the atmosphere, which, in turn, influences the formation and lifecycle of clouds [27,28]. ALH plays a key role in the direct and indirect radiative forcing of aerosols, which is required for calculating Earth's energy budget [29–31]. Moreover, it can help identify and trace the long-range transport of aerosols, shedding light on their lifecycle and enabling the monitoring of air quality to forecast severe air pollution events [32]. The retrieval of ALH depends on the observing wavelength, as detailed in previous studies [11, 33]. In the discussion section, the calculated minimum heights corresponding to different observational wavelengths are presented.

This study extends previous work by utilizing twilight radiometry beyond 1000 nm, allowing for more precise aerosol layer height detection. By integrating advanced radiative transfer modeling techniques and improved observational datasets, a more robust method for stratospheric aerosol analysis has been presented. Previous studies, such as [34], proposed a simple analytical expression for twilight brightness. This expression has now been compared with radiative transfer (RT) simulations under clear sky conditions, both including and excluding ozone, as illustrated in Figure 4. All RT calculations were performed using the libRadtran package [24, 35]. For RT simulations in twilight (i.e., for solar zenith angle ($90° < \mathrm{SZA} < 100°$), the Monte Carlo solver MYSTIC has been used [24]. It is a fully spherical code that takes the spherical geometry of the Earth into account without simplifying assumptions [36]. With the help of this model, layer height information at different wavelengths is investigated and discussed. Comparisons of AODs on different days between the ResPan instrument and collocated AERONET (AErosol RObotic NETwork) measurements during daylight, at various SZAs, are presented in Section 5. Additionally, comparisons between ResPan and MERRA-2's (Modern Era Retrospective Analysis for Research and Applications-2) [37] AOD at 550 nm are also discussed. For daylight conditions (i.e., for $\mathrm{SZA} < 90°$), the DISORT RT code (pseudospherical from $80° < \mathrm{SZA} < 90°$) from the libRadtran package [24] has been used. Furthermore, the impact of the Hunga Tonga volcanic eruption on aerosol loading is explored, with data from the ResPan instrument at the Lauder site used to study aerosol layer heights in comparison to SAGE and lidar measurements.

The paper is organized as follows: Section 3 describes the adopted method; Section 4 outlines the data used; Section 5 presents the results; Section 6 provides an analysis of the results; Section 7 summarizes the conclusions reached of this study; Section 8 provides the analytical methods and Section 9 provides the calibration procedures applied in this study.

3 Twilight Radiometry

Twilight radiometry provides a method for estimating aerosol properties based on light scattering during twilight conditions. When the Sun is below the horizon, the upper part of Earth's atmosphere is illuminated, and the lower part is partly obscured by Earth's shadow. The scattering due to molecules, ozone and aerosol particles above this boundary causes the twilight sky brightness. The lowest atmospheric layer, which is the densest, contributes most to the scattering and can thus be measured by detecting the shadow height corresponding to the twilight SZA. The twilight radiometry method can cover a wide range of altitudes. Volcanic eruptions enhance the stratospheric aerosol layer loading at certain altitudes. The twilight brightness method, as discussed previously in many works, [11–13, 33, 38, 39] has been used to study and retrieve the optically active constituents of Earth's atmosphere.

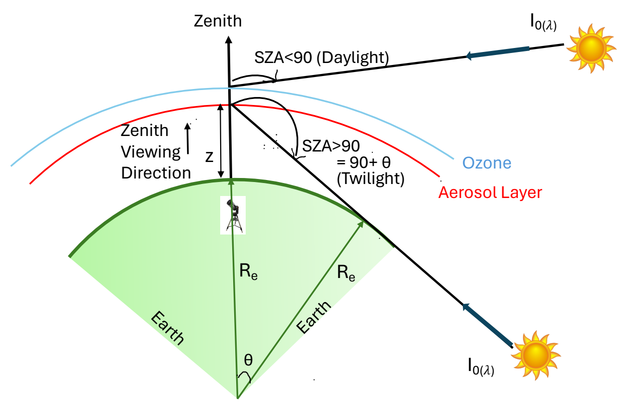

Figure 1: Schematic representation of daylight and twilight geometries with aerosol and ozone layer.

Figure 1 shows the geometry of the two cases studied in this work. Daylight occurs when SZA$<90°$ (when solar rays passes the Earth's atmosphere), and twilight occurs when the SZA$>90°$ (when solar rays graze Earth's surface). Both cases use a zenith viewing direction where R_e is the radius of Earth, θ is the depression angle, and $I_{0(\lambda)}$ is the incident intensity. The geomteric shadow height (z) is from the surface of Earth where the line of sight and rays grazing the Earth meet shown in Figure 1. When this ray hits the aerosol layer (red) this particular height becomes key to the aerosol layer height information. In the diagram, the ozone layer is shown in blue. As solar light passes the Earth's atmosphere, it undergoes wavelength dependent attenuation and molecular scattering. Additionally, absorption due to water vapor and ozone is present as well. Therefore, the geometric shadow is defined as the shadow height which Earth would cast if it had no atmosphere [40]. In previous works, the effective height of Earth's shadow derived from the visible range included a screening height added to the geometric shadow height. An expression for the effective Earth's shadow height was suggested as z + $(20/\sin\theta)$ km, and $20/\sin\theta$ is the screening height by [41]. Later, it was suggested to add 11 km for 450 nm and 3 km for 650 nm to account for the screening height [40, 41].

The geomteric Earth's shadow height, excluding the screening height, z, (as shown in Figure 1) for zenith viewing can be computed as :

$$z = R_e(\sec\theta - 1), \tag{1}$$

where R_e and θ are same as discussed before. If longer wavelengths (¿650nm) are used for observation then the Earth's shadow height would be very close to the geometric shadow height of the lowest grazing rays also mentioned in earlier work [7]. This is confirmed by computation done using various wavelengths where longer wavelengths are able to detect the aerosol layer height well, which is close to the geometrical shadow height of the lowest grazing rays as shown in Figures 13 and 14 as well as in Table 1. Early twilight studies initially used wavelengths up to around 650 nm. It was not until later that longer wavelengths, extending to approximately 800 nm, were introduced into twilight observations [12]. This study, to the best of the authors' knowledge, represents the first application of twilight radiometry beyond 1000 nm wavelengths, providing new insights into aerosol layer heights at stratospheric altitudes. The deductions are compared with other lower wavelengths.

An expression for the brightness of the sky with the Earth's atmosphere both with pure air and air with ozone was presented in the work [34]. The expression for clear sky with and without ozone is verified first and then subsequently compared with the radiance calculated by Monte Carlo RT code [24]. The brightness expressions are given in the appendix (Section 8) and the comparison outcomes are presented in the result (Section 5). The impact of single versus multiple scattering at different ranges of wavelength are also highlighted.

To study the relationship between aerosol properties (AOD and ALH), the RT code is simulated at different SZAs and wavelengths. The wavelengths 450, 550, 762, 775 and 1050 nm are used as part of this study. For the aerosol model, Gaussian-shaped stratospheric aerosol layers have been implemented in the model atmosphere at mean altitudes, 5, 10, 15, 20, 30, and 40 km with variance of the distribution of 0.85 (close to 1). A minimum mean altitude of 5 km was chosen in this study to explore the limits of the twilight radiometry method. The stratospheric aerosol optical thickness (at $\lambda = 550$ nm) ranged from $\tau = 0.003$, 0.005, 0.008, and 0.01. The Sun is treated as a point source, and convolution of the solar zenith angle with half a degree is not performed.

This work uses the ratio of intensity/radiance at two wavelengths, also known as the color ratio method, to identify aerosol properties (AOD and ALH). In the past this method has been successfully used to detect AOD [38, 39] using different wavelength ratios. The method is based on the characteristic wavelength dependency of scattering by particles. For instance, Rayleigh scattering predominates at shorter wavelengths, whereas aerosol scattering is more significant at longer wavelengths. Based on this fact, the ratio of the intensities at 775 nm and 450 nm is found to be useful to infer the aerosols' ALH and AOD information. The Oxygen-A band is commonly used to retrieve aerosol height information [42–46]. Oxygen is a well mixed gas in the atmosphere and because of its pressure dependence it can provide reliable vertical information of aerosol [46]. This is possible because the oxygen-A band's absorption gets modified by the multiple scattering caused by aerosols at various altitudes [44]. The Oxygen-A band wavelength has been used for remote sensing with satellite based as well as ground based instruments [47]. Particularly, the wavelength 762 nm is chosen from oxygen-A band. The relationship between the ratio of 775 nm and 450 nm and difference of 775 and 762 nm has been explored. It is found to provide consistent and reliable information about ALH as well as AOD. The band at 550 nm is used to inspect the aerosol information as it corresponds to the peak of the solar spectrum and the mid visible range where the radiative effect is highest [48]. The Ångström exponent equation is:

$$\tau(\lambda) = \beta\lambda^{-\alpha} \tag{2}$$

where $\tau(\lambda)$ is the aerosol optical depth (AOD) at wavelength λ, β is the turbidity coefficient, and α is the Ångström exponent. If AOD at two wavelengths are known (λ_1 and λ_2) using eq. (2), α can be calculated as:

$$\alpha = -\frac{\ln\left(\frac{\tau(\lambda_1)}{\tau(\lambda_2)}\right)}{\ln\left(\frac{\lambda_1}{\lambda_2}\right)} \tag{3}$$

Thereafter AOD at an unknown wavelength (λ) can be obtained as:

$$\tau(\lambda) = \tau(\lambda_1)\left(\frac{\lambda}{\lambda_1}\right)^{-\alpha} \tag{4}$$

AERONET's spectral AODs at 440 and 675 nm were used to obtain the Ångström exponent and the AOD at 550 nm using eqs. (2)–(4), which was then compared to MERRA-2's AOD at 550 nm. The twilight method is applied to show that the aerosol layer height as low as 5 km can be detected with help of longer observing wavelengths. The height limitation is imposed by the attenuation of atmospheric layers closer to the Earth's surface. The SZA (around 94°) corresponding to height of 20 and 30 km have been used to demonstrate the twilight theory. Direct-Sun measurements perform well for SZA until 80°, but zenith-sky measurements allow for extended spectral measurements, which help provide aerosol height information. Ordinarily, during twilight with a non-turbid atmosphere, the intensity decreases rapidly with increase in height and with increase in SZA. However, the presence of the aerosol layer leads to increased scattering, which manifests as a peak in the intensity versus SZA plot. This method of detecting the aerosol layer was first proposed [41]. Following this concept, the logarithmic gradient of intensity (where intensity is measured in relative units), $q(\lambda, z)$, calculated from the rate of change in intensity with height, is a key method to detect the aerosol layers based on their scattering properties:

$$\mathrm{q}(\lambda, \mathrm{z}) = \mathrm{dlogI}_{(\lambda)}/\mathrm{dz} = \mathrm{dI}_{(\lambda)}/\mathrm{I}_{(\lambda)}\mathrm{dz}. \tag{5}$$

The z is the vertical height or Earth's shadow height corresponding to the solar depression angle θ as used in Figure 1 and dI_λ is the corresponding change in scattered intensity. As mentioned before, the scattered intensity also depends on the wavelength of observation. Molecular scattering and ozone absorption diminish with increasing wavelength, which makes aerosol scattering a relatively more significant contributor. Consequently, longer wavelengths in the near-infrared range are particularly useful for retrieving aerosol properties. The atmospheric refraction has been neglected in this work.

In previous studies of twilight simulations, the pseudospherical DISORT RT code was used, which incorporates Chapman functions to account for the Earth's curvature [12, 38]. However, it was realized that for higher SZAs or a low Sun, the pseudospherical correction is not sufficient. In such cases, a fully spherical solver—such as a Monte Carlo model—is required [13,24,36]. The models used in this work is from the libRadtran package, which is a library of various RT routines and programs [24,35]. The Total and Spectral Solar Irradiance Sensor (TSIS) solar spectrum has been used for the solar input [49]. For twilight simulations starting from a solar zenith angle (SZA) of 90°, the MYSTIC solver is used [50]. For SZAs between 80° and 90°, the DISORT solver with a pseudo-spherical approximation is preferred, as it is significantly faster than MYSTIC while still providing comparable accuracy when the Sun is above the horizon.

For RT simulation with SZA $\leq 80°$, the DISORT solver is used [51]. The Monte Carlo method is subject to statistical noise, but MYSTIC does not use any simplifying assumptions or approximations to solve the radiative transfer equation as shown in [**?**]. Therefore, it does not introduce any bias which has been confirmed by various comparisons with independent radiative transfer solvers and by comparison with observations. The statistical noise in the Monte Carlo based RT simulations are reduced by using 1×10^9 photons. Moreover, the derivative method used in the paper would not be affected by a constant offset factor, since you calculate dI/I.

For the Greenbelt location, an urban surface was adopted in the model, while grassland was used as the corresponding surface type for the Lauder location.

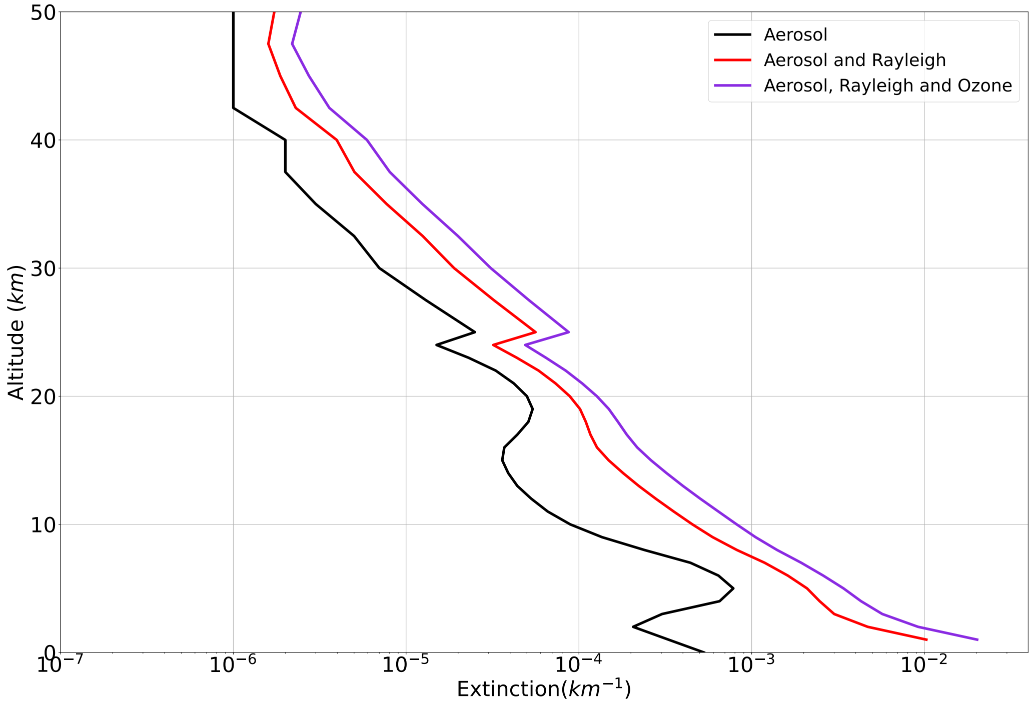

Figure 2: Background Aerosol Profile With AOD at 550 nm as 0.005.

Figure 2 shows the background aerosol, Rayleigh and ozone profile used in the RT model as part of this work [24]. The model employs the US Standard Atmosphere 1976, as implemented in the libradtran package [24]. The atmospheric composition used in the model is based on the paper [52], which includes molecules such as ozone, oxygen, water vapor, carbon dioxide, and nitrogen dioxide as its constituents. For the aerosol peak at 20 km and 30 km, the aerosol profiles used are Figure 3a and Figure 3b respectively.

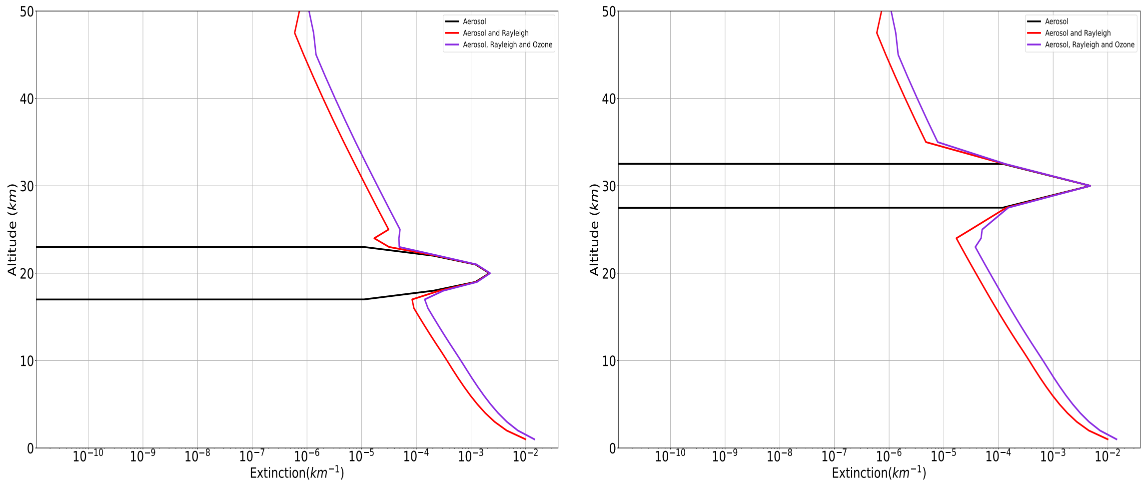

(a)

(b)

Figure 3: Aerosol Profile With Gaussian Peak (3a) at 20 Km (3b) at 30 Km.

4 Data

The Pandora spectrometer is a ground-based instrument designed to perform measurements under both daylight and twilight conditions. Developed under a NASA initiative in 2005, it operates on the differential optical absorption spectroscopy (DOAS) principle to quantify atmospheric trace gases. Pandora instruments are deployed globally as part of the Pandonia Global Network (PGN) (https://www.pandonia-global-network.org, last access: 6 September 2024; [53, 54]), which supports atmospheric validation efforts. Two widely used models include the Pandora-1S (280–530 nm) (https://sciglob.com/pandora-1s/, last access: 6 September 2024) and the Pandora-2S (270–900 nm) (https://sciglob.com/pandora-2s/, last access: 6 September 2024), both of which are employed in diverse research applications.

In this work, ResPan, which is an extended wavelength ranged Pandora has been used. The ResPan instrument was originally developed by the Pandora network group at NASA (National Aeronautics and Space Administration)/GSFC (Goddard Space Flight Center) [25]. Most of the components of ResPan are similar or identical to the standard Pandora instrument, except for the spectrometer. ResPan is regularly used with direct-Sun observations to retrieve trace gases like O_3, NO_2, and H_2O and aerosol properties like single scattering albedo, aerosol optical depth, and mean radius [25]. As part of this work, zenith viewing geometry has been used while taking measurements by ResPan. The same geometry has also been used while implementing the libRadtran model to obtain the aerosol's AOD and ALH information using the twilight method for the first time. The instrument units used in this study are registered as ResPan-43 (set up at Lauder, New Zealand) with a wavelength range of 310 to 830 nm and ResPan-48 (set up in Greenbelt MD) with a wavelength range of 310 to 1100 nm. Prior to field deployment, these ResPan spectrometers underwent spectral calibration using known solar and atmospheric lines, as well as radiometric calibration at the GSFC Grande facility. The Grande calibration provided the conversion coefficient that translates spectrometer count measurements into radiances for each channel. Calibration details are presented in the appendix (Section 9)

AOD computed by ResPan is compared to AERONET's Version-3 Level 1.5 with improved cloud screened data (https://aeronet.gsfc.nasa.gov, last access: 6 September 2024) [55,56]. AERONET is a network of ground based sun photometers operated throughout the world providing various aerosol properties established by NASA. However, as a surface-based instrument, AERONET has spatial and temporal limitations, particularly when clouds obscure its field of view. The estimated uncertainty in the AOD computed by AERONET primarily due to calibration is approximately $\sim 0.010 - 0.021$ [56]. The ResPan model uses the ozone data from Giovanni (Geospatial Interactive Online Visualization ANd aNalysis Infrastructure) [57], MERRA-2 [37] data. Additionally, the AOD data from MERRA-2 is compared with the AOD retrieved by ResPan using zenith view radiance observations. MERRA-2 is the reanalysis data by NASA's Global Modeling and Assimilation Office (GMAO).

Twilight data obtained from the ResPan-43 instrument deployed at Lauder, New Zealand, following the Hunga Tonga eruption, is used to illustrate the aerosol height information and is compared to collocated Stratospheric Aerosol and Gas Experiment (SAGE) III measurements. SAGE III, onboard the International Space Station (ISS), performs sunrise and sunset occultation measurements of aerosols and gas concentrations in the stratosphere and upper troposphere, providing vertical profiles of aerosol extinction at different wavelengths [18–20].

Twilight photometry provides a simple, cost-effective method for providing aerosol profiles from 3 to 200 km. While the method is qualitative and lacks the precision of lidar profiles, it has proven to be more stable than filter-based instruments, which can degrade over time [58]. A simple but effective twilight photometer was developed in 2013 following experiments at the Mauna Loa Observatory. These instruments provide atmospheric profiles of tropospheric dust, smoke, and air pollution from 3 km to the stratospheric aerosol layer (SAL) at 15–20 km, as well as profiles of aerosols from major volcanic eruptions above the SAL. During meteor showers, these instruments provide profiles of meteor smoke at 80-95 km within the mesosphere and cosmic dust at in the lower thermosphere. Detailed information on the design and assembly of these twilight photometers is available [59].

The data used to illustrate the aerosol layer height information in this work is from a significantly improved light emitting diode (LED) twilight photometer developed by Hagerup Technical Services in 2022 for a National Aeronautics and Space Administration (NASA) project. This photometer was designed to measure the altitude of aerosols from the historic Hunga Tonga eruption, which occurred from December 20, 2021, to January 15, 2022. Previous LED photometers used a simple slit method to control the instrument's field of view. The Hagerup version mounted the LEDs at the base of a 150 mm tube capped by a 25 mm diameter lens installed in a 100-mm lens tube capped by a 25 mm lens. This configuration offers a very narrow field of view—just 0.3°, enabling high-resolution aerosol profiling while significantly minimizing interference from stars [59].

The twilight data from the 1050 nm photometer is compared to JPL's lidar data from the Table Mountain Facility, CA (TMF) [60]. For aerosol backscatter data, TMF Stratospheric Ozone Lidar (TMSOL) [61] is used, while the TMF Water Vapor Raman Lidar (TMWAL) [62] is used for water vapor mixing ratio volume backscatter. TMSOL combines Rayleigh/Mie and nitrogen vibrational Raman scattering techniques, whereas TMWAL exploits vibrational Raman scattering of nitrogen and water vapor molecules.

Finally, twilight data from the ResPan instrument at the Greenbelt site is used to illustrate aerosol/cloud height information and is compared to collocated MPLNET (Micro-Pulse Lidar Network) measurements [63]. Version 3 MPLNET lidar data were used here to provide information on atmospheric vertical structure and aerosol height and backscatter properties [64]. MPLNET data are available online at https://mplnet.gsfc.nasa.gov.

5 Results

5.1 Model Simulation

To understand the physics of twilight sky brightness, the analytical twilight model has been compared with the modern Monte Carlo RT code from libRadtran's package [24].

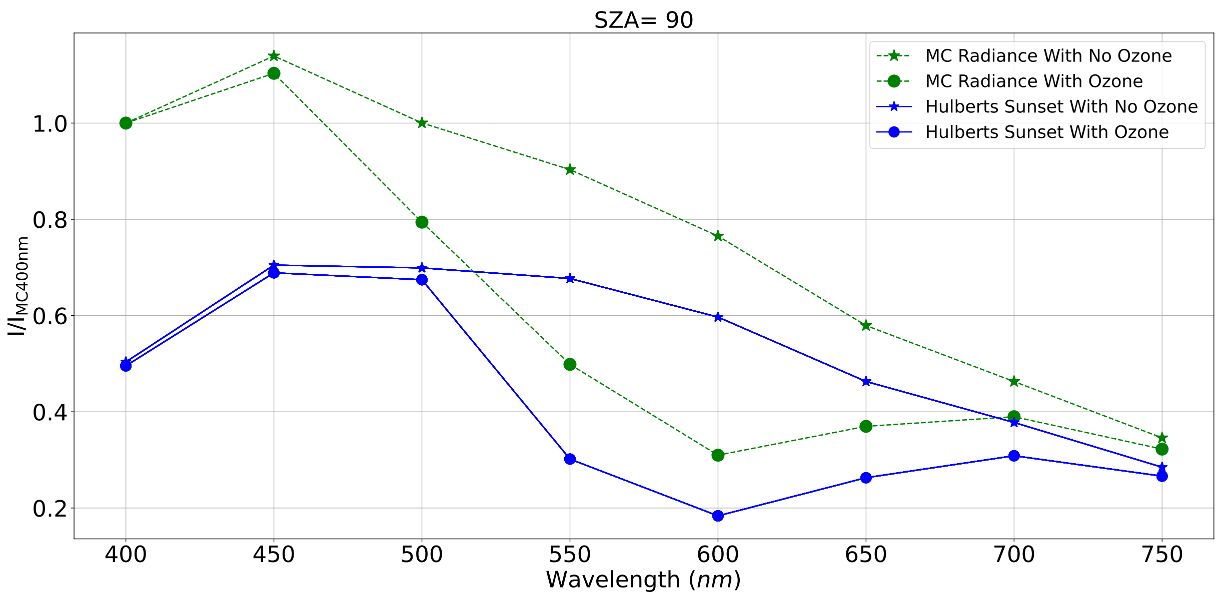

Figure 4: Comparison between Hulbert's sunset [34] and Monte Carlo Radiance [24].

Figure 4 shows the comparison between the ratios $I/I_{MC_{400}}$ as obtained from MC RT code and the analytical sunset model at SZA = 90° (Equation (6)) where the viewing zenith angle is 0°, looking up from the ground. Two types of atmospheres are considered: one with molecular scattering only, and the other with both Rayleigh scattering and ozone absorption. The ozone profile in the analytical model is adopted from [34], while the MC RT model uses the one provided in the libRadtran's package [24] is used. For ease of comparison between the two models, both MC RT and the anaytical model are normalized by RT's radiance at 400 nm for both with and without ozone cases [34]. The models show greater differences at shorter wavelengths, where Rayleigh scattering dominates, compared to longer wavelengths. Particularly, the atmosphere with only Rayleigh scattering has higher radiance when calculated by the MC RT model compared to the analytical model . This difference gradually decreases towards longer wavelengths. The analytical model takes into account only the single scattering whereas the RT model includes both single and multiple scattering. Consequently, there is more scattering in the MC RT model compared to the analytical model due to the predominance of molecular scattering at shorter wavelengths by Rayleigh particles. Furthermore, when the atmosphere has both Rayleigh and ozone contribution, the absorption by the Chappius band of ozone is noticed in both models.

For the rest of this work, the Monte Carlo RT model from libRadtran [24] is used to describe the twilight conditions and DISORT for daylight. For twilight conditions, radiance at higher SZAs ($> 90°$)needs to be calculated. This requires investigating the validity of RT codes' simulations for corresponding SZAs. Hence the limitations of DISORT and Monte Carlo were investigated for the twilight conditions. In the Figure 5 the irradiance computed by both RT codes is compared for SZAs 85°, 90°, and 94°. In this comparison, irradiance is used instead of radiance due to the high computational cost of Monte Carlo radiative transfer (MC RT) simulations for radiance calculations. From SZA 91° onwards, the two codes differ significantly. With background aerosols, the difference between DISORT and Monte Carlo is less than 5% for SZA between 85° and 89°. The error approaches 8% for SZA= 90° and worsens beyond that. Although DISORT is faster compared to Monte Carlo, it is not accurate at higher SZAs [36], as it assumes a pseudospherical atmosphere.

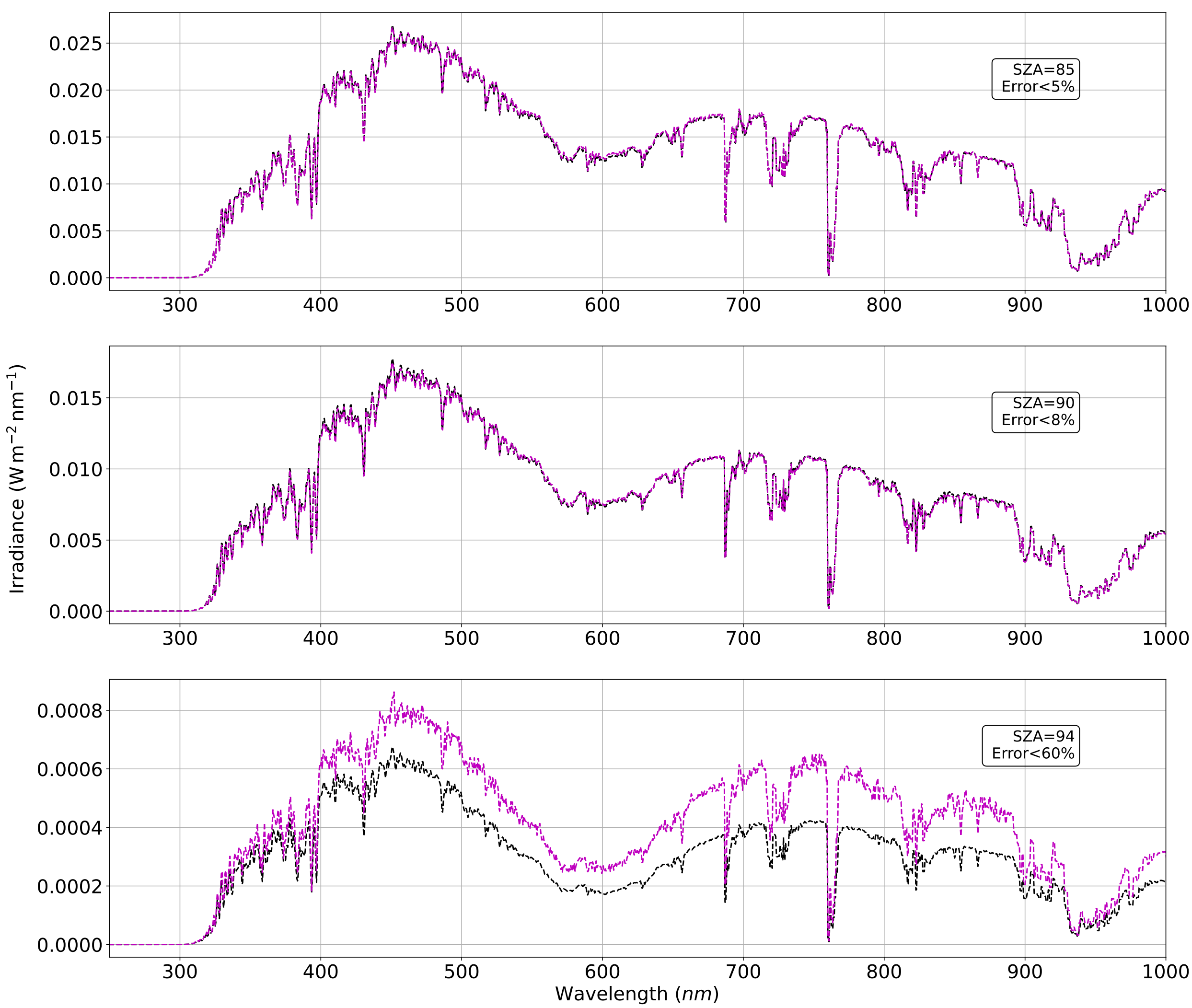

Figure 5: Comparison between Pseudospherical Disort (in Black) Vs Monte Carlo (in Magenta) at SZAs 85°, 90°, and 94°.

To confirm the accuracy of Monte Carlo in twilight conditions, the radiance computed by the model was compared to data from ResPan deployed in Greenbelt, MD, on December 12, 2023, with SZA ranging from 85° to 100°. This includes civil twilight and a significant portion of nautical twilight. The model radiance computed by Monte Carlo for four wavelengths (450, 762, 775, and, 1050 nm) in the Figure 6a are found to be similar to ResPan data shown in the **??**. The model simulations used the default setting for atmospheric aerosol and trace gas profiles, to illustrate the variation with respect to SZA. The strong agreement between the model and ResPan data supports the accuracy of the Monte Carlo simulations under twilight conditions. Convolution of the solar zenith angle by half a degree would slightly alter the slope but would not affect the final outcome. This comparison was part of an exercise aimed at evaluating the shape of the observations relative to the model, rather than achieving an exact retrieval.

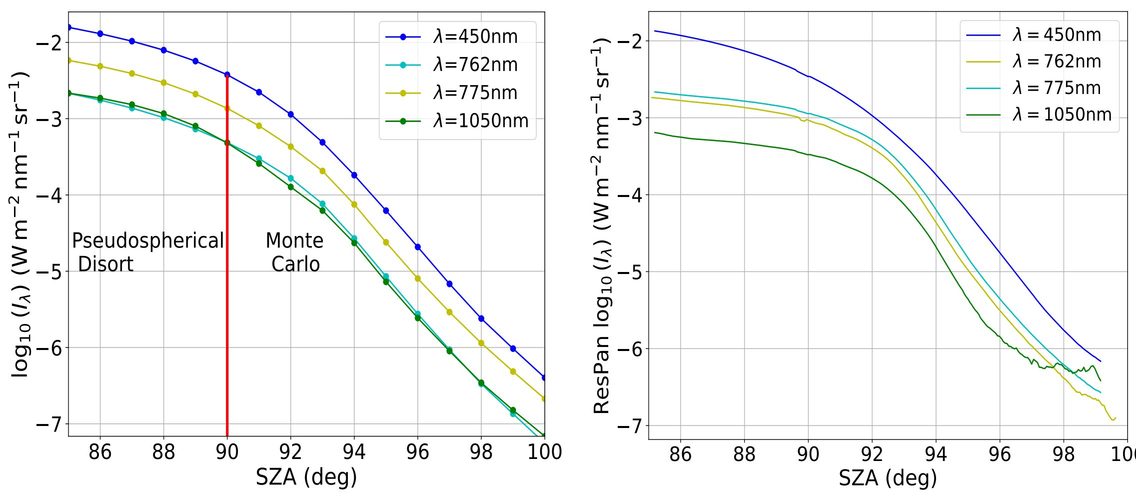

(a) Model (b) ResPan Data

Figure 6: Comparison of twilight radiance as a function of solar zenith angle (SZA) between (6a) Monte Carlo model simulations (6b) and ResPan observational data.

5.2 Daylight

For the daylight model, the DISORT RT code of libRadtran [24] with pseudospherical geometry has been used to investigate the dependence of scattered intensity on AOD and ALH for SZA = 85° and results are shown in the Figure 7. Two different ALH (20 and 30km) and increasing stratospheric AOD (from 0.003 to 0.01) have been implemented. Scattered intensity increases with aerosol optical depth. The aerosols with similar AODs are close to each other with very less distinction between different layer heights. The aerosols at same height irrespective of their AODs seem to follow the same slope indicating that it does not have aerosol height information. The color ratio method is found to be dependent on the surface information (further described in ground surface section 5.5) as well as the calibration of the instrument (for the x-axis). This analysis is based on the radiative transfer model MYSTIC, which does not introduce any inherent error. However, when applied to actual data, uncertainties may arise. The associated horizontal error corresponds to an absolute uncertainty of 5%, while the vertical error is estimated to be approximately 10%. Implementation of the method using actual data is part of future work. The spectral ratio and its associated propagated uncertainties are defined in (Section 9).

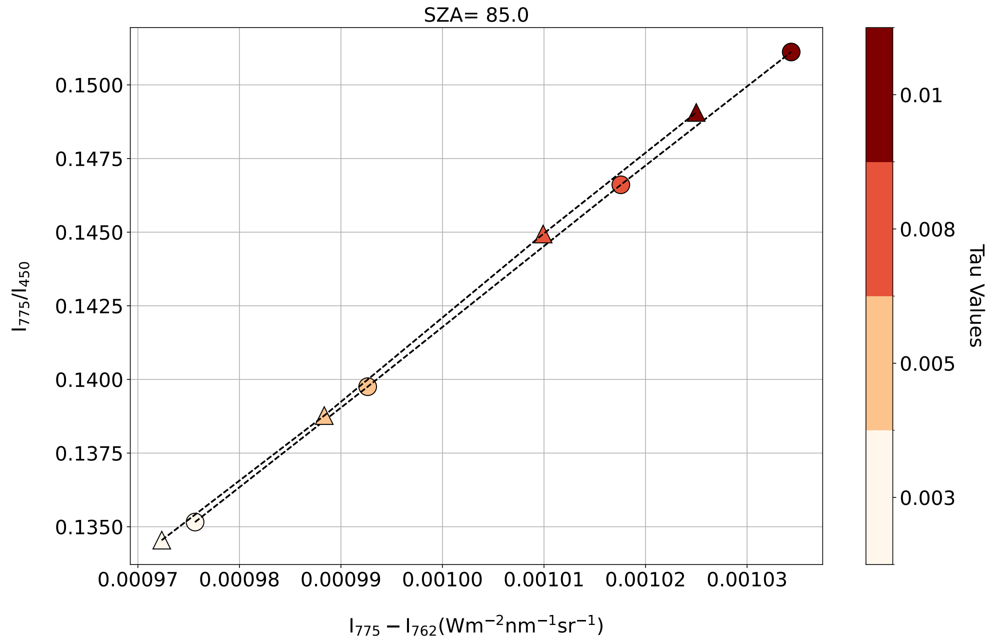

Figure 7: Ratio of I_{775} and I_{450} vs difference of I_{775} and I_{760} (7) at SZA=85°. The circles indicate ALH=20 km and triangles indicate ALH=30 km with increasing AODs.

Furthermore, AODs retrieved using ResPan data are compared to collocated AERONET AOD measurements at the NASA/GSFC site. The results are shown in the Figure 8a. The ResPan-48 spectra were scaled by ±5% to account for potential calibration errors and instrument degradation after the deployment. This scaling factor is applied to all ResPan-48 data and the AOD retrievals. The date 12th December 2023, with an SZA of 70° in the plot, has been taken as the reference point for these comparisons. The ozone concentration has been adopted from MERRA-2's hourly NASA data. Different colors in the plot represent different dates. The slope is 1.04 and the Pearson correlation coefficient or R-value is 0.99. Some of the cases retrieved by ResPan don't agree well with AERONET. AOD from ResPan is also compared to MERRA-2 data in the Figure 8b for same dates and SZAs showing a slope of 0.34 and R-value of 0.86. To demonstrate the technique employed by ResPan with zenith view, SZA of 65.2 (Dated: 12th December 2023) from Figure 8a is selected. The corresponding AERONET's AOD at 550 nm (0.035) for SZA=65.2 is found with help of Ångström coefficient computed by AOD at 500 and 675 nm wavelengths. Based on this information, a range of AODs (0.030 to 0.045) and ozone information for the corresponding UTC taken from MERRA-2, are used to compute different corresponding atmospheric models. Thereafter, the code chooses the AOD (0.033 in this case) such that the error is least between the corresponding model and observation. The residual plot is shown in the Figure 9a. The spectral range affected by Fraunhofer lines was (shown in the Figure 9a) avoided during spectrum matching between the model and observational data for Aerosol Optical Depth (AOD) retrieval to minimize errors.

The comparison plot between model and observation is shown in the Figure 9b where blue represents the model whereas red represents the observation data from ResPan-48. ResPan-48 has not been calibrated from 300 to 400 nm and hence this wavelength range is avoided here. For error minimization, the wavelength range from 500 to 660 nm is chosen. This is because lower wavelengths have ozone's dominating contribution and higher wavelength have surface contributions (Section 5.5).

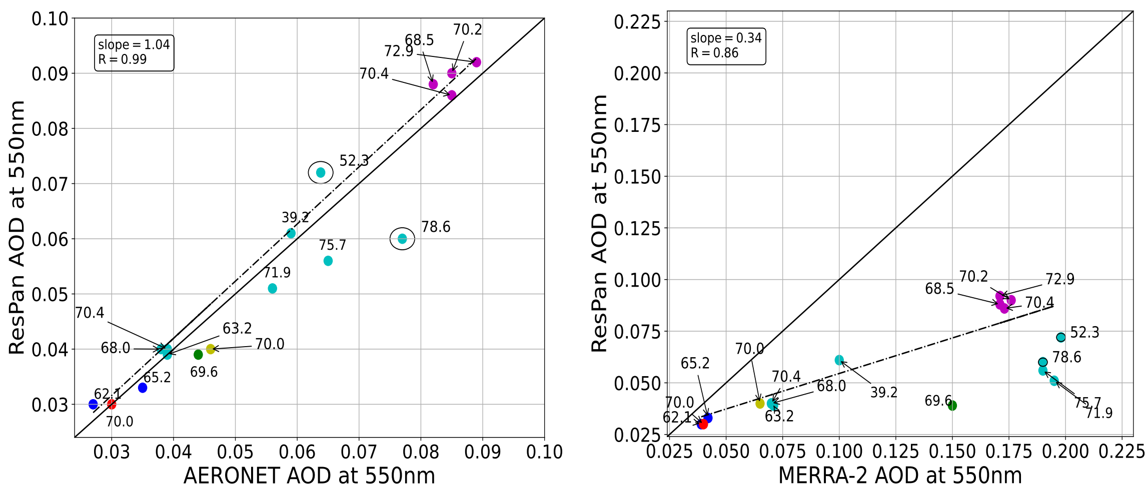

(a)

(b)

Figure 8: Comparison between Pandora measurements vs AERONET (8a) and vs MERRA-2 (8b).

To understand the differences between AODs calculated by the two instruments (ResPan and AERONET), March 21, 2024, was chosen as it includes both good and poor agreement points. On this date (marked by the cyan dots in the plot 8a), AODs from AERONET and ResPan-48 agree well for most SZAs. The SZAs studied on this day are 39.2, 52.3, 63.2, 68.0, 70.4, 71.9, 75.7 and 78.6.

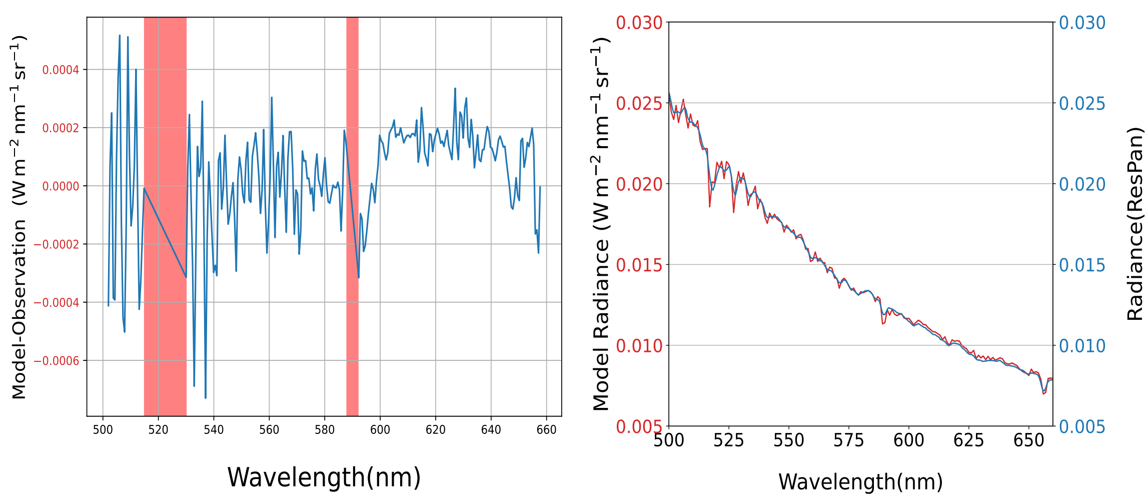

(a)

(b)

Figure 9: AOD Retrieval using Pandora measurements and DISORT model (9a) Residual plot and (9b) Comparison plot, between data and model.

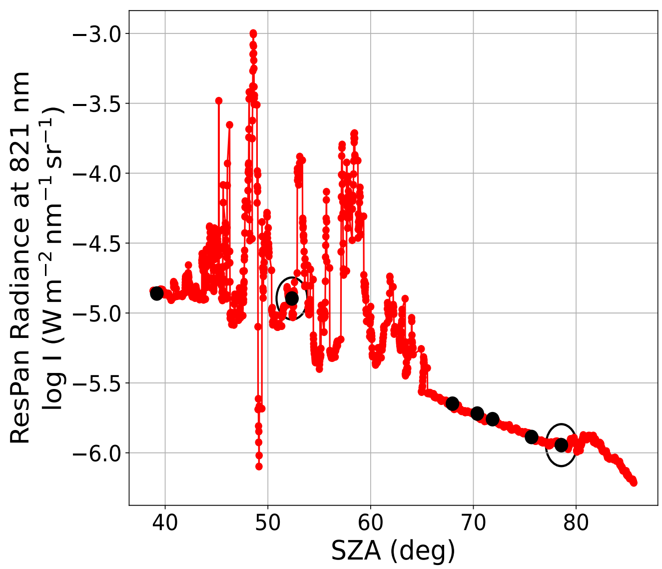

Figure 10: Radiance at 821 nm for March 21, 2024, in Greenbelt, MD.

The radiance data from ResPan-48 at 821 nm (Figure 10) has been chosen to understand the reason behind the poorly agreeing SZA cases shown in Figure 8a. The two SZAs (52.3 and 78.6) on March 21, 2024, show variability over time in the radiance plot. (Figure 10) which can suggest cloud in the field of view of the instruments. Similar methods are adopted to detect clouds in the field of view of the instrument, as described in the work [65]. One of the reasons for the differences in AODs measured by the two instruments can be attributed to their different viewing geometry. AERONET uses direct sun measurements and then performs air mass factor correction to yield zenith view equivalent AOD whereas ResPan, as part of this work, uses zenith viewing geometry. Additionally, the deviation in the two measurements can be due to a cirrus cloud in the instruments' field of view. The different temporal scatter of the radiance around SZA = 52.3° and 78.6° suggests thicker clouds in the first case as shown in Figure 10.

An overestimation of MERRA-2 AOD values has been observed, particularly when the actual AOD is low [**?**]. These measurements were taken during colder months, a period when AOD levels in Greenbelt are typically low, and MERRA-2 struggles to capture the local and seasonal variations as effectively as AERONET. This discrepancy may be attributed to several factors, including generalized background aerosol levels, limitations in satellite data assimilation under low aerosol conditions, inaccuracies in aerosol type representation, and differences in temporal and spatial resolution between the MERRA-2 model and AERONET observations.

The next section investigates the twilight sky using similar methodologies.

5.3 Twilight

For the twilight model, the dependence of scattered intensity on AOD and ALH is investigated using the Monte Carlo RT code from libRadtran [24], and results are shown for SZA = 94° in Figure 11. Larger AODs result in higher scattered intensities, and the distinct

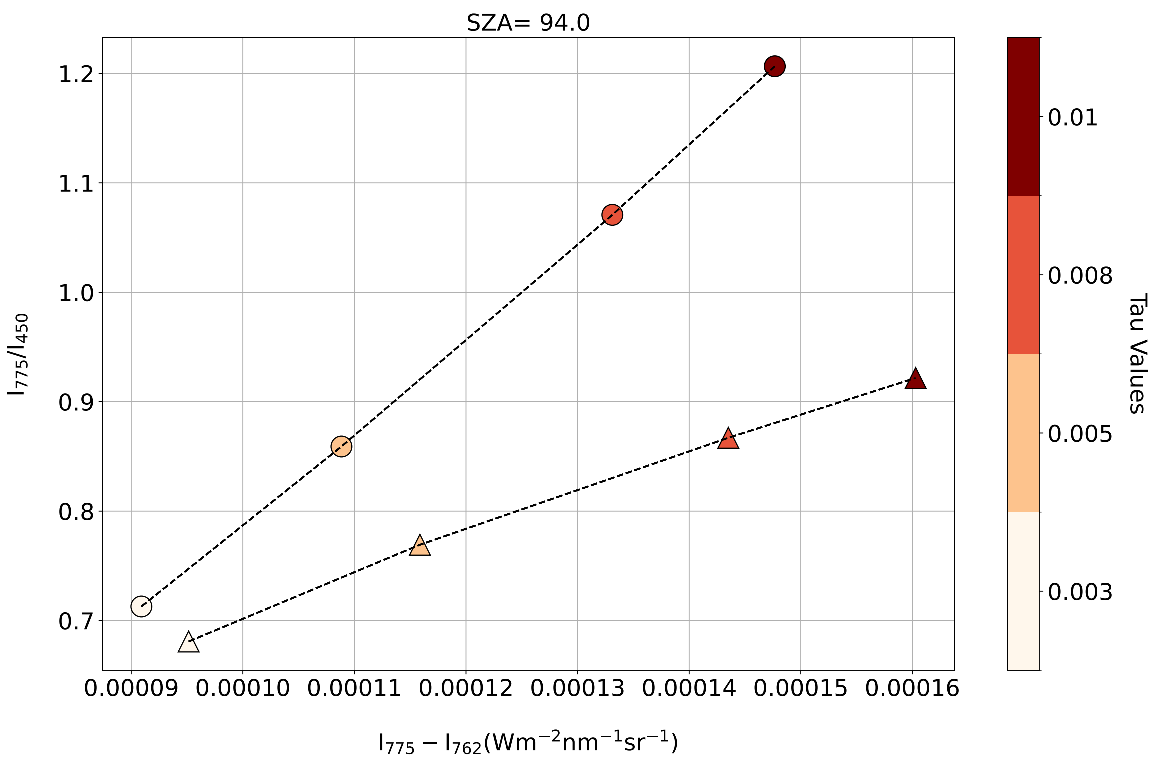

Figure 11: Ratio of I_{775} and I_{450} vs difference of I_{775} and I_{760} at SZA=94°, using Monte Carlo simulations.

slopes corresponding to different layer heights confirm that height information can be retrieved using the twilight radiometry method. At higher solar zenith angles during twilight, when sunlight interacts with aerosols at an altitude of around 20 km, relatively less blue light (450 nm band) is scattered downward. In contrast, when the light interacts with an aerosol layer at a higher altitude, such as 30 km, more blue light is scattered downward. As a result, aerosol scattering at different heights produces distinct slopes in the computed color ratios. This feature can be used to infer the aerosol layer height at higher solar zenith angles (SZAs), as demonstrated in Figure 11.

Furthermore, to illustrate the sensitivity of twilight spectrum to different aerosol AOD and their heights, irradiance spectra are computed separately with background aerosols as given in Figure 2 and for different AODs at a height of 30 km. The computations are done by Monte Carlo for SZA=94° (Figure 12). This highlights that, in the presence of background aerosols or aerosols with low AOD at higher altitudes (e.g., 30 km), the second peak at 775 nm in the twilight spectrum is comparable in intensity to the first peak at 450 nm. However, as the AOD increases, the second peak becomes more pronounced and eventually surpasses the first peak in intensity. This behavior indicates that the relative intensity of these two wavelengths can be used to approximately infer the altitude and optical depth of the aerosol layer.

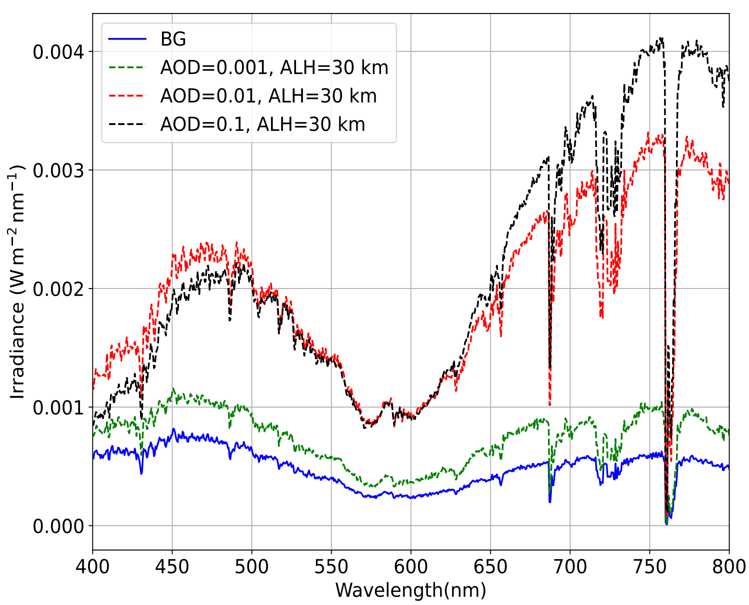

Figure 12: Modeled irradiance spectra for different aerosol optical depths (AODs) at 30 km altitude using Monte Carlo simulations.

Another method to infer the aerosol layer height is the computation of logarithmic gradient of intensity (q), shown in Figures 13 and 14. For this exercise, two aerosol layer heights and three wavelengths, namely the 550, 775, and 1050 nm, with an AOD equal to 0.005 at 550 nm, are considered. The left side plots show how the negative of q behaves with respect to the SZAs, and the right side plots show the relationship between mean height and negative q. In the left plots, a spike is observed at a particular SZA, and this corresponds to Earth's shadow height, suggesting scattering due to aerosol. The right side plots also show a spike at the height where the intensity increases due to scattering by aerosol at that specific height. In Figure 13, where the aerosol layer height is at 20 km, it can be seen that 775 and 1050 nm contain the aerosol height information, whereas 550 nm does not show such details. For higher aerosol heights (Figure 14), the logarithmic gradient of intensity at 550 nm starts showing some sensitivity towards the ALH but is not well defined compared to longer wavelengths (775 and 1050 nm).

To demonstrate how aerosol height influences radiance at higher solar zenith angles (SZAs), Figure 15 presents spectra obtained from ResPan measurements at the Lauder, New Zealand site on 28th May 2024. The blue spectrum shows morning data, whereas the red shows afternoon data. The afternoon spectrum shows a peak at 775 nm compared to the morning data, suggesting the presence of an aerosol layer. This is similar to the irradiance plot (Figure 12), where a high AOD shows a peak at 775 nm as well. Thus, it is evident from Figure 15 that the height information of aerosols is present in the radiance at higher SZAs.

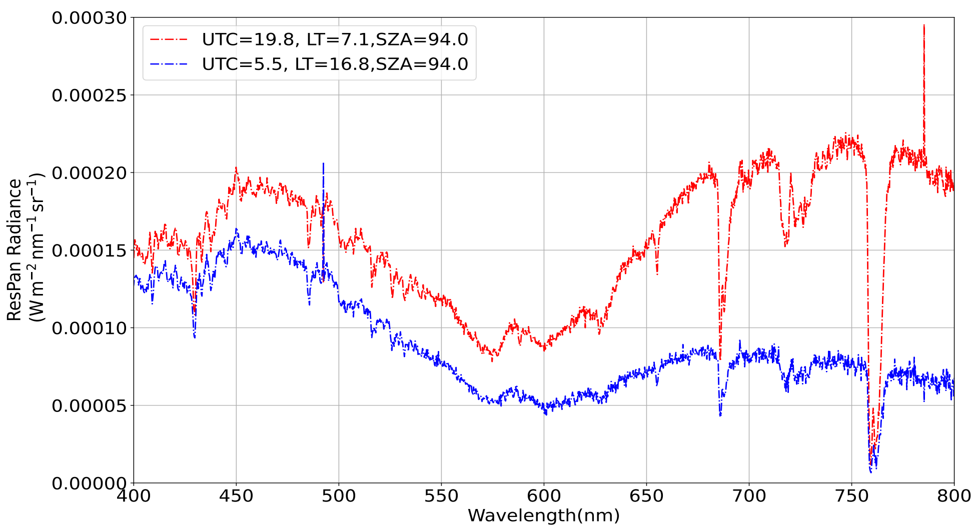

Figure 15: Comparison of Afternoon(Red) vs Morning (Blue) radiance from Lauder, New Zealand.

The two methods (color ratio and derivative) discussed above are used to detect the aerosol layer height from data collected by ResPan-43, deployed in Lauder, NZ. November 26, 2022, was chosen because it followed the Hunga Tonga volcanic eruption, allowing for the observation of aerosol injection into the stratosphere. The Figure 16a is similar to previous Figure 11. Here, the model (indicated in the plot) with an ALH at 25 km is compared to data obtained from four different days/twilights. To include bending due to atmospheric refraction, a half degree difference in SZA is considered between the model (SZA=93.5°) and the observation (SZA=94°). With this addition, the color ratio corresponding to model simulation for the aerosol layer at 25 km comes closer to the ResPan twilight data. The twilight of November 26, 2022 (indicated in red in Figure 16a) was investigated by the derivative method as well (Figure 16b). In the derivative method, aerosol height is detected both with (indicated in red) and without refraction (indicated in black). Bennett's empirical formula

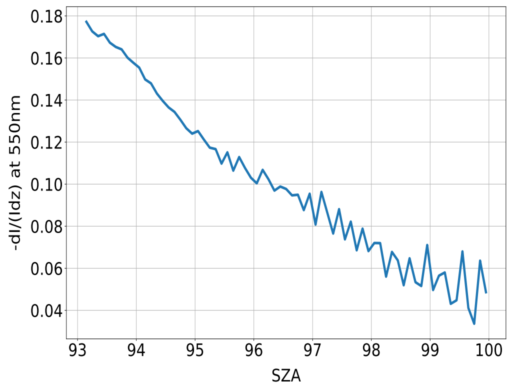

(a) -dI/(Idz) versus Solar Zenith Angle at 550 nm.

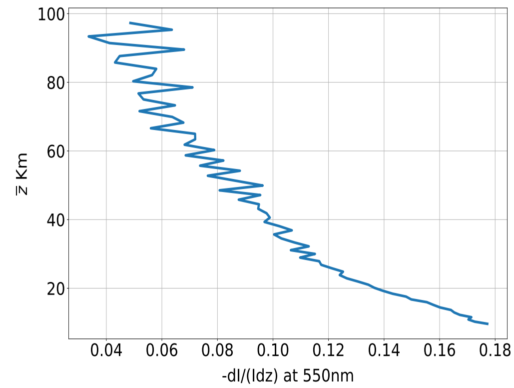

(b) Mean Height versus -dI/(Idz) at 550 nm.

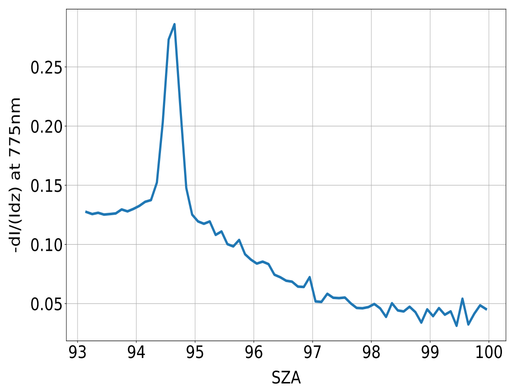

(c) -dI/(Idz) versus Solar Zenith Angle at 775 nm.

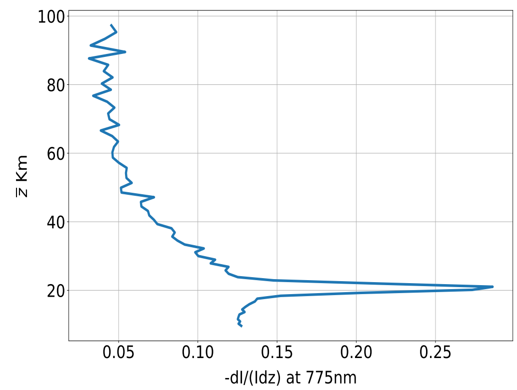

(d) Mean Height versus -dI/(Idz) at 775 nm.

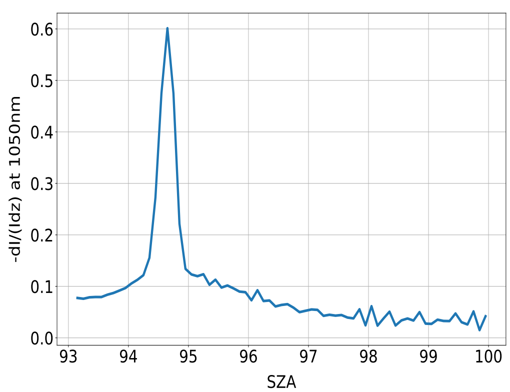

(e) -dI/(Idz) versus Solar Zenith Angle at 1050 nm.

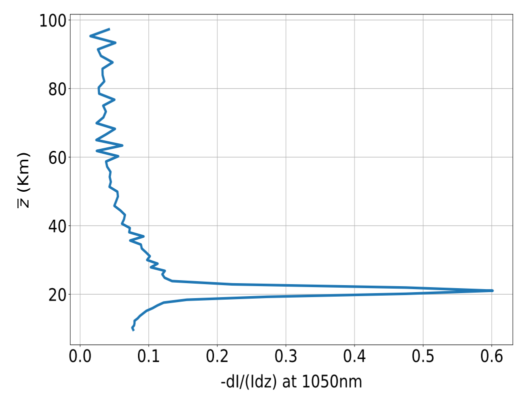

(f) Mean Height versus -dI/(Idz) at 1050 nm.

Figure 13: Illustrations of the aerosol peak at 20 km with an AOD of 0.005 at 550 nm, using Monte Carlo simulations.

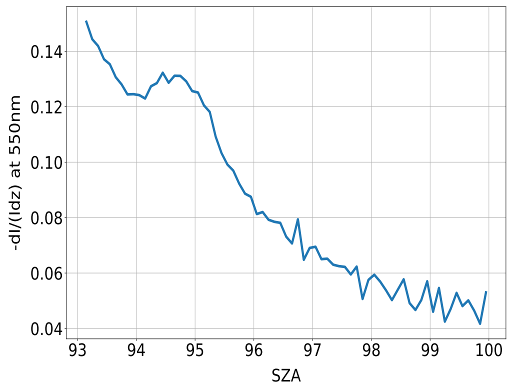

(a) -dI/(Idz) versus Solar Zenith Angle at 550 nm.

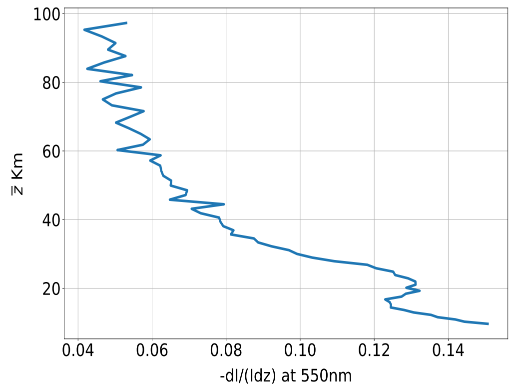

(b) Mean Height versus -dI/(Idz) at 550 nm.

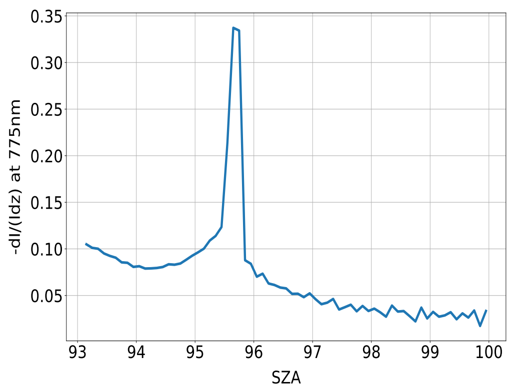

(c) -dI/(Idz) versus Solar Zenith Angle at 775 nm.

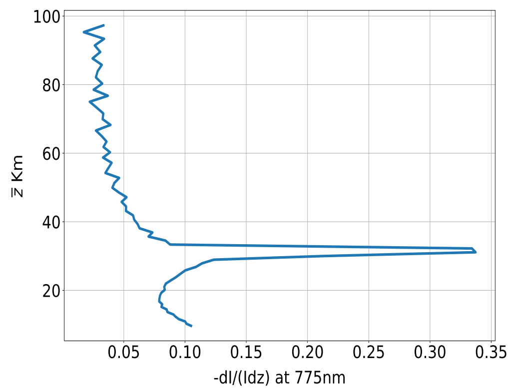

(d) Mean Height versus -dI/(Idz) at 775 nm.

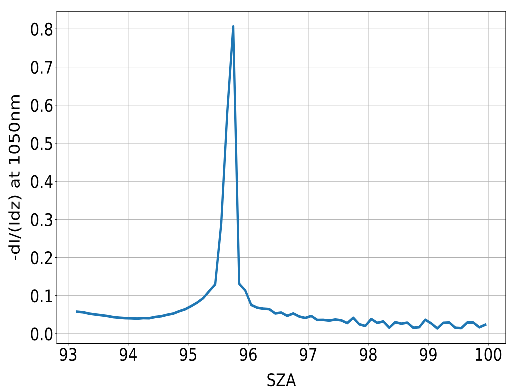

(e) -dI/(Idz) versus Solar Zenith Angle at 1050 nm.

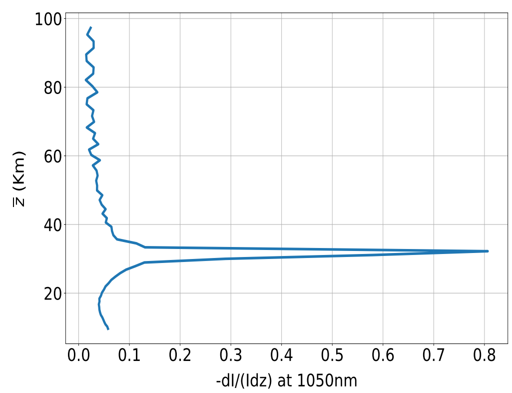

(f) Mean Height versus -dI/(Idz) at 1050 nm.

Figure 14: Illustrations of the aerosol peak at 30 km with an AOD of 0.005 at 550 nm, using Monte Carlo simulations

has been incorporated [66] to include the refraction due to Earth's atmosphere. Without refraction, the detected height is 28 km, which is higher than the 23 km detected when refraction is included. On the same day lidar data were obtained from Lauder (Figure 17) [67], as well as SAGE data (Figure 25). Both indicate an aerosol layer at a height of approximately 18 km. This shows a difference of 5 km compared to the ResPan prediction of the aerosol layer height. This difference can be primarily attributed to atmospheric refraction. Improved refraction models can help reduce this difference.

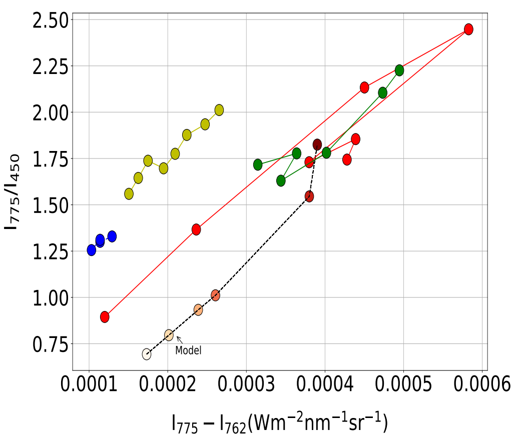

(a)

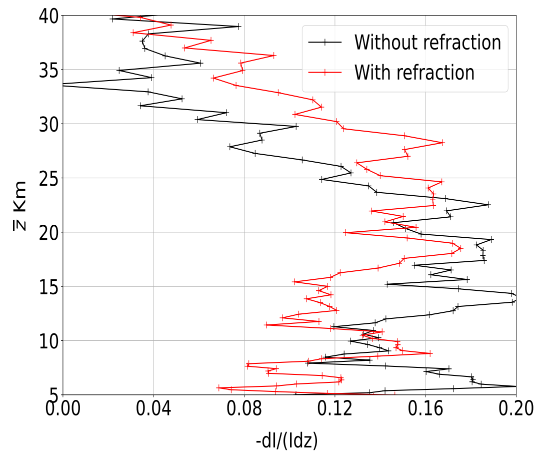

(b)

Figure 16: ResPan data at 775nm used to estimate aerosol layer height (ALH) using two methods, (Figure 16a) the color-ratio method, showing observational data compared with a model at 25 km ALH and (Figure 16b) the derivative method, detecting ALH both with and without refraction effects.

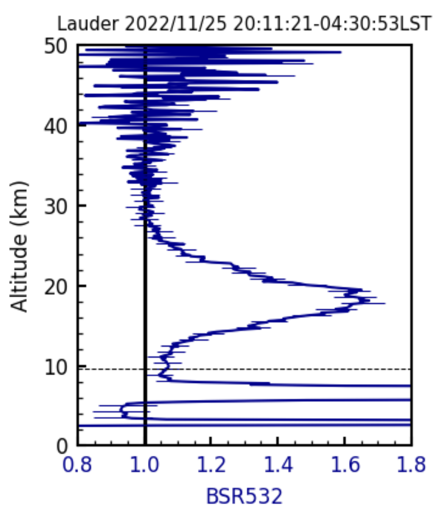

Figure 17: Vertical distribution of the aerosol backscatter ratio at 532 nm (BSR532) observed over Lauder on November 25, 2022. The horizontal dotted line indicates the tropopause.

5.4 Twilight Photometer

The method is further applied to twilight photometer data from Brea, California, and subsequently compared to JPL lidar data from Table Mountain, CA. The comparison is shown in Figure 18. The photometer shows aerosol peaks at approximately 4, 18, 26, and 37 km altitudes (Figure 18c). This is compared with JPL data, which is not collocated but is about 70 miles away. Since the aerosol backscatter data from JPL has a minimum cutoff of 15 km, for the aerosol layer comparison below 10 km, JPL's H_2O volume mixing ratio is used. Previous works have shown a positive correlation between the aerosol backscattering ratio vertical profiles and the water vapor mixing ratio [68].

The photometer shows four aerosol peaks at approximately 4, 18, 26, and 37 km altitudes. Similar aerosol peaks can also be observed in the JPL's aerosol lidar profile (> 10km) (Figure 18a). In the Figure 18b, H_2O volume mixing ratio has a peak around 6.5 km, approximately, which is similar to photometer's peak at 5 km. The aerosol layer around 5-7 km can be attributed to long-range transported finer dust particles. A similar aerosol loading was also reported using measurements from MPLNET in a publication [69].

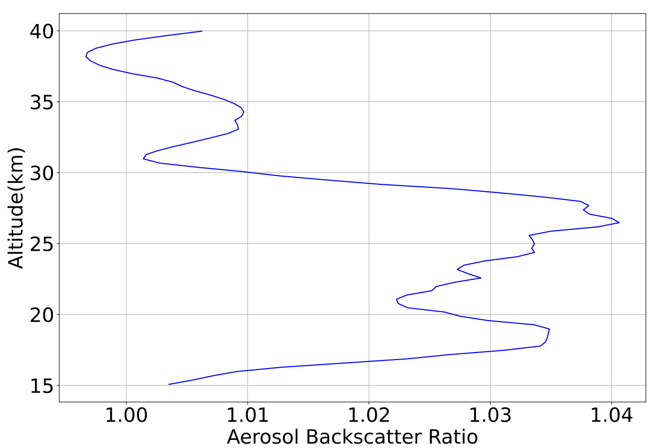

(a) JPL Aerosol Backscatter ratio versus altitude, Table Mountain, California.

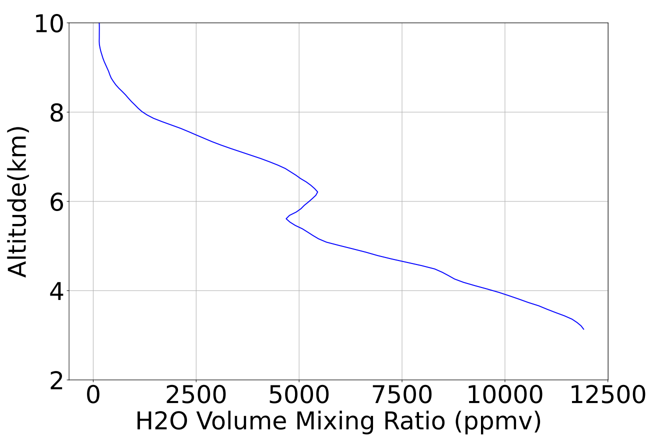

(b) JPL H_2O Volume Mixing Ratio versus altitude, Table Mountain, California.

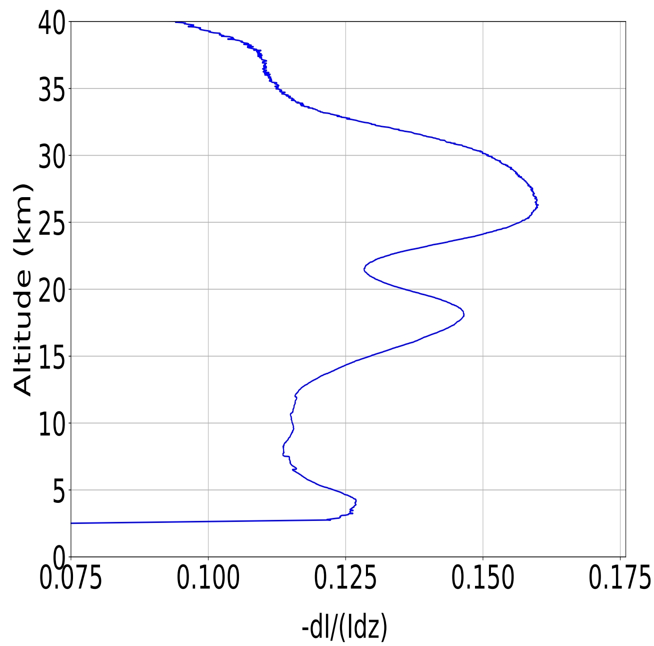

(c) Mean Height versus -dI/(Idz), Brea,California.

Figure 18: JPL Data (Figures 18a and 18b), Table Mountain, CA, and Twilight Photometer (Figure 18c) from June 25, 2024, Brea, CA.

Zenith view geometry is chosen in this work because it can provide continuous measurements through twilight and is also advantageous for retrieving near-surface species [23]. Additionally, it can be sensitive to ground surface reflectance as shown in Figure 19.

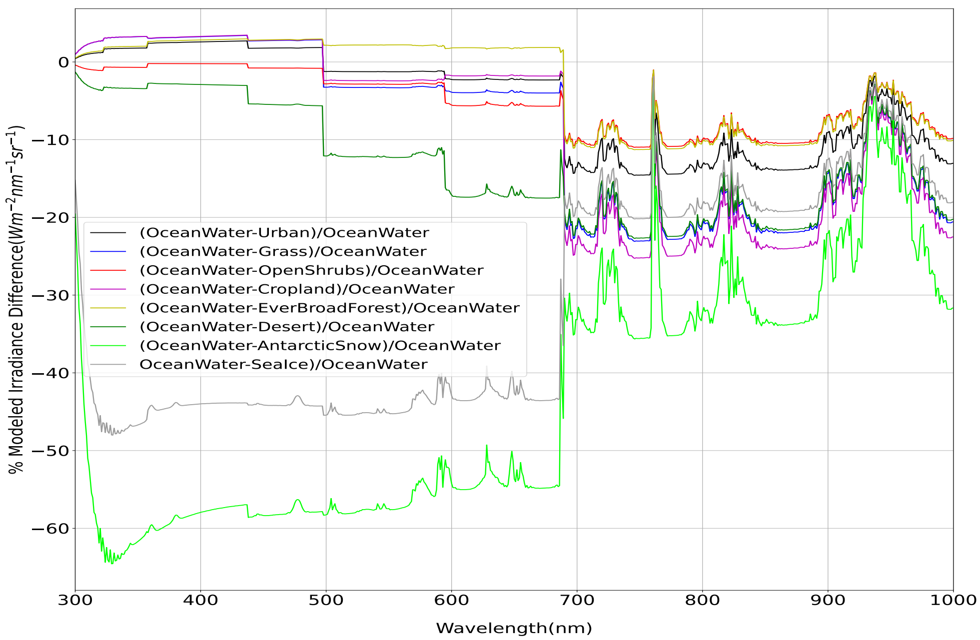

Figure 19: Comparison of modeled irradiance with different surfaces, using DISORT simulations.

5.5 Surface

Figure 19 presents the percentage differences in the model radiance computed by DISORT at an SZA of 70° with a zenith viewing geometry for various surfaces available in the libRadtran package [24]. Most surfaces—except deserts, sea ice, and Antarctic snow—show noticeable percentage differences at wavelengths of 700 nm and beyond when observed from a zenith viewing geometry. Therefore, for wavelengths above this threshold, AOD retrievals may be influenced by assumptions about the surface type. A comparison between the zenith-view and direct Sun geometries reveals the impact of the surface on AOD retrievals. Consequently, a zenith-view geometry at wavelengths above 700 nm can be used to infer information about the surface type.

6 Discussions

The accurate detection of ALH also depends on the wavelength at which twilight sky brightness is observed. The results are presented in the Table 1. The logarithmic gradient of intensity (q) at different wavelengths of observation can help determine the layer height. Table 1 presents the results for aerosol layer heights at 5, 10, 15, 20, 30, and 40 km with AOD = 0.005 at 550 nm, at three separate wavelengths (550, 775, 1050 nm) using the derivative method. When aerosols are at lower altitudes, the longer wavelengths are more effective in

	TRM Height Prediction at Wavelengths (nm)		
Aerosol Peak Height (Km)	550	775	1050
5.0	-	-	5.5
10.0	-	-	11.0
15.0	-	-	17.42
20.0	-	21.03	21.03
30.0	20.0	29.34	30.30
40.0	32.0	39.86	40.57

Table 1: Comparison of Aerosol Peak Prediction at different Wavelengths with AOD=0.005 at 550 nm

detecting their height. For instance, at 5, 10, and 15 km, only 1050 nm was able to detect the presence of the aerosol layer. Although ALH at 20 km is detected by 775 and 1050 nm, it is not detected at 550 nm. However, for ALH higher than 20 km, using 550 nm as the observation wavelength can still detect a layer, although not as accurately as longer wavelengths, as shown in Figures 13 and 14. These results confirm that longer wavelengths should be preferred for detecting ALH at lower altitudes. Shorter wavelengths (like 550 nm) consistently predict the height to be lower than the actual value. This supports the use of a screening height assumption at lower wavelengths, as done in earlier works [40, 41]. This discrepancy is largely due to the stronger Rayleigh scattering and absorption from the Chappius band of ozone (450–700 nm) at shorter wavelengths, which causes a loss of aerosol information. At longer wavelengths, these effects are weaker, making it easier to detect aerosol properties. The sensitivity of the second aerosol peak to AOD and height at higher wavelengths is also evident in Figures 12 and 15. The same derivative method was used to detect the background aerosol profile presented in Figure 2 with AOD=0.005 at 550 nm, using 1050 nm. As shown in Figure 20, the method successfully detects the peak at 5 km using Monte Carlo simulations.

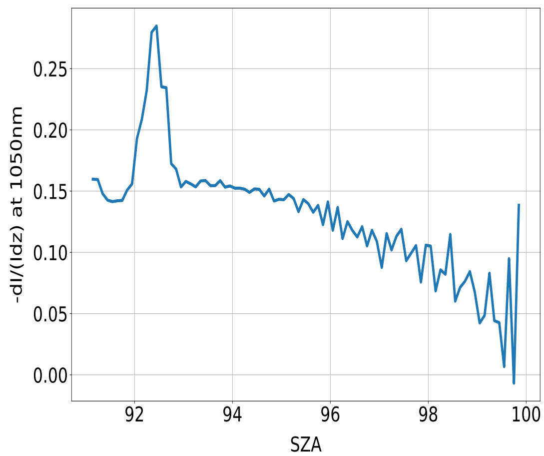

(a) Mean Height versus -dI/(Idz) at 1050 nm with Background aerosols.

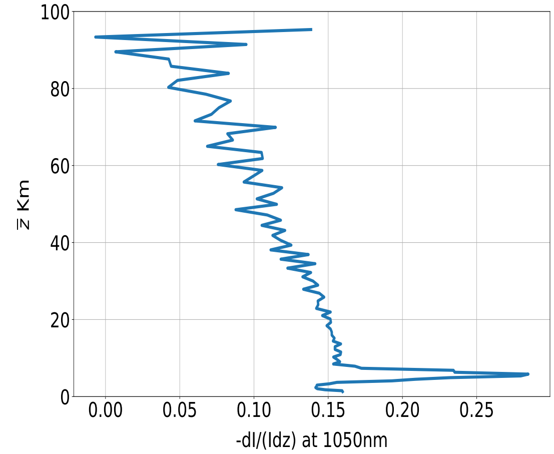

(b) -dI/(Idz) versus Solar Zenith Angle at 1050 nm with Background aerosols.

Figure 20: Background aerosol detection by derivative method.

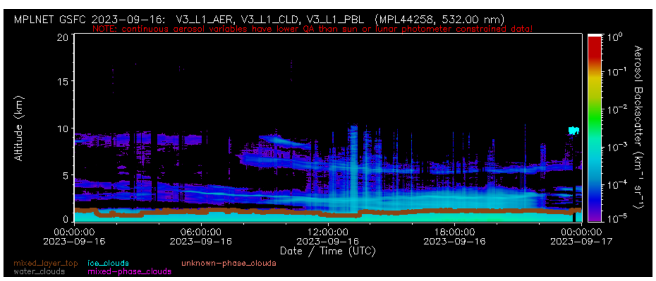

(a) MPLNET Aerosol Backscatter plot.

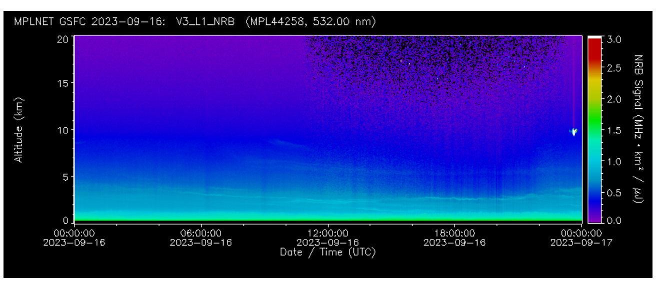

(b) MPLNET Normalized Relative Backscatter Signal plot.

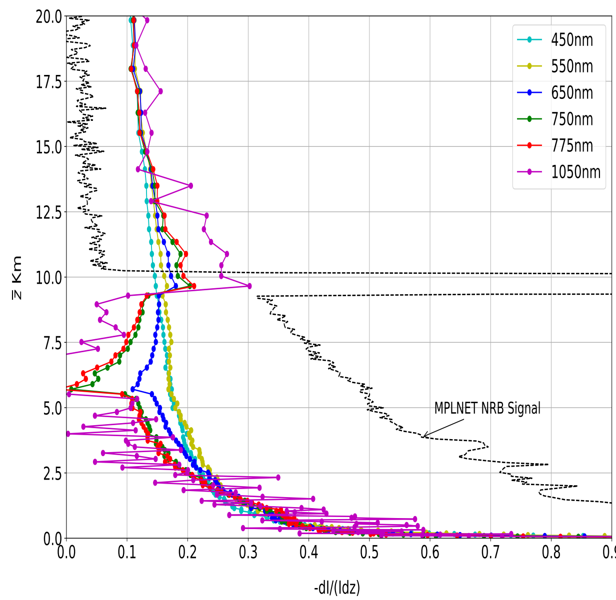

(c) Mean Height versus -dI/(Idz).

Figure 21: MPLNET Data (figs. 21a and 21b), and ResPan (fig. 21c) from September 16 2023, Greenbelt, MD.

Additionally, the method was applied to data from a clear day, using spectrometer measurements from ResPan-48 deployed at Greenbelt, MD, on September 16, 2023. Figure 21c shows that the derivative method was able to detect the peak due to broken cloud at wavelengths of 775 and 1050 nm, with a smaller peak at 550, and 650 nm, but no peak at 450 nm. Although the spectrometer used here was somewhat noisy at 1050 nm (as shown in **??**), it still managed to capture the peak. Figure 21c shows that the peak in the derivative plot is highest at 1050 nm and gradually decreases as the wavelength decreases. The decreasing intensity of the peak can be attributed to the loss due to absorption by Chappius band of ozone and Rayleigh scattering. The cause of the peak was further investigated using MPLNET data from the same date as shown in the Figure 21. The MPLNET data predicts the peak as ice-cloud (Figure 21b) at around 23.36 UTC. Both instruments detected the broken ice-clouds from approximately 23.36 to 23.45 UTC. This is further confirmed by camera images in the **??**. Here, in the **??** shows the scene before cloud cover, the **??**, shows when the cloud is in the crosshair, and the **??** shows when the cloud has passed.

This exercise shows that ice-cloud with backscatter magnitude about 10^{-3} can be detected by the derivative method as shown in the Figure 21c. Very low AODs ($< 10^{-3}$) and lower heights were not observed even by 1050 nm wavelength. As part of this analysis, the ResPan prediction is very close to the MPLNET data, even without including the bending due to refraction. Atmospheric refraction bends light more at higher altitudes, where longer paths are traveled.

7 Conclusion

Twilight brightness influences many processes on Earth, with the different colors during twilight resulting from scattering by air molecules, aerosols, and ozone. The brightness at a given time is further influenced by the height of Earth's shadow, which can be used to interpret stratospheric aerosol properties. Stratospheric aerosols play a significant role in Earth's climate, both regionally and globally. While satellite measurements provide valuable data on stratospheric aerosols, they require validation through complementary ground-based and airborne measurements. To address this need, the twilight radiometry method was introduced. This method uses the simple geometry of Earth's shadow to determine aerosol peak height, providing a useful tool to corroborate satellite data. Existing literature highlights several limitations of the twilight radiometry method, including restricted wavelength ranges, lower accuracy in measuring twilight radiance, and limited observational datasets. This work makes significant advances in the understanding of twilight radiance and its potential as a tool for atmospheric monitoring. The study provides valuable insights into the role of aerosols in climate dynamics, air quality, and the Earth's radiative balance, offering a novel approach to studying atmospheric properties through twilight observations.

As an initial step, the twilight brightness analytical method has been verified [34]. For simulations at higher SZAs between 90° and 100°, the Monte Carlo RT model has been shown to be close to observations made by spectrometer whereas DISORT with pseudospherical geometry agrees with observational data up to an SZA of 90° with background aerosol. The Gaussian distribution of the aerosol layer is preserved when longer wavelengths are used to obtain ALH information. At shorter wavelengths, absorption by ozone and molecular scattering can modify the height of Earth's shadow, making them less sensitive to aerosol properties. In contrast, longer wavelengths provide more information. To obtain ALH, two methods are proposed: the color ratio and derivative methods. In both cases, wavelength selection is of immense importance. Shorter wavelengths are affected by Rayleigh scattering and gas absorption, whereas longer wavelengths are more sensitive to aerosol properties. Although the color ratio method depends on surface information and instrument calibration, it can be complemented by the derivative method to confirm the retrieved aerosol height. The derivative method can detect the aerosol layers as low as 5 km using longer wavelengths, with detection at lower heights depending on the observed wavelengths.

The computation of AOD from radiance measured by ResPan using zenith viewing geometry has been discussed. Its agreement with AERONET (Direct-Sun measurements, R = 0.99) and MERRA-2 (model, R = 0.86) demonstrates the homogeneity of the aerosol layer. Cloud screening can be achieved by monitoring rapid changes in the radiance measured by ResPan. The twilight data also distinguish between high and low AOD in specific wavelength ranges. The close agreement between aerosol height information obtained from the twilight data by ResPan-43, deployed in New Zealand after the Hunga Tonga eruptions, and that from SAGE and collocated lidar data further supports the method. The aerosol height information obtained using this method from ground measurements can serve as a valuable tool to confirm ALH data from instruments like SAGE.

One of the proposed future directions of this study is to use the derivative and color ratio methods for retrieving aerosol height. Pandora spectrometers are widely deployed worldwide, and these data can be utilized to predict the aerosol layer height using the twilight method. This would result in a global data product capable of resolving many global climate dynamics. Future work will refine refraction models and expand the application of twilight radiometry to trace gases, with a focus on ozone studies in the UV portion of the spectrum. Additionally, GOES-R imagery will be used to investigate the potential of the twilight method for predicting cloud heights.

8 Appendix A

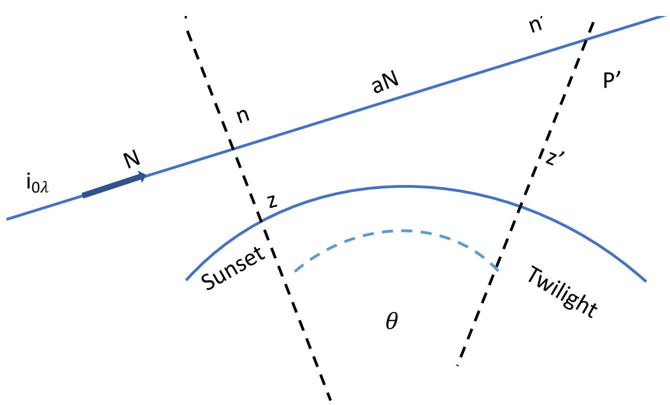

Figure 22: Twilight Geometry [34]

For brightness calculation at sunset Hulbert proposed the following expression [34]:

$$\mathrm{B}(\lambda) = \mathrm{i}_{0\lambda}\frac{\sigma_{90^\circ\lambda}}{\sigma_\lambda}\frac{\mathrm{H}}{\mathrm{K}-\mathrm{H}}\mathrm{e}^{-\sigma_\lambda \mathrm{H} \mathrm{n}_0}[1-\mathrm{e}^{-\sigma_\lambda(\mathrm{K}-\mathrm{H})\mathrm{n}_0}], \tag{6}$$

where $\mathrm{i}_{0\lambda}$ is the solar radiance and its values are used from Total and Spectral Solar Irradiance Sensor (TSIS) [49]. H is the scale height and is taken as 7 km, K is $\sqrt{(}\pi r\mathrm{H}/2)$ and n_0 is the molecular density on the surface. $\sigma_{90^\circ\lambda}$ is the scattering coefficient per air molecule per steradian at 90° and σ_λ is the scattering cross-section per air molecule. The $'\beta'_\lambda$ notation in Hulbert's paper is the scattering cross section and has been represented in the modern notation as $'\sigma_\lambda'$ in this paper. For brightness calculation at twilight Hulbert used the following expression [34]:

$$B(\lambda) = i_{0\lambda} \frac{\sigma_{\theta\lambda}}{\sigma_\lambda} \frac{H}{2AK - H} e^{-\sigma_\lambda H n_0} [1 - e^{-\sigma_\lambda (2K - H/A) n_0}], \tag{7}$$

where $A = \exp(r\theta^2/2H)$ and θ is the depression angle.

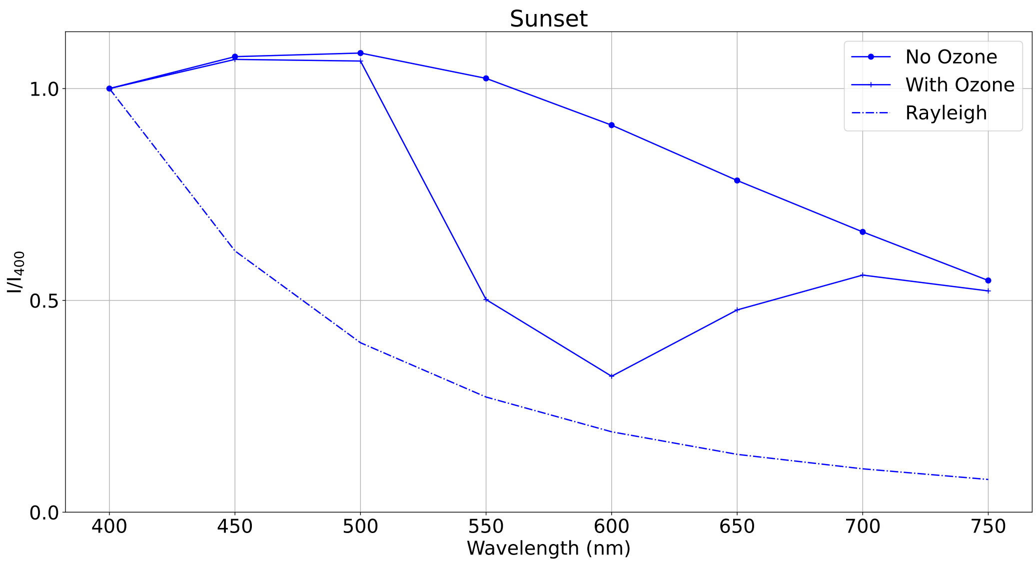

Figure 23: Hulbert's sunset Model.

9 Appendix B

The calibration procedure involved spectral characterization/registration and radiometric correction as detailed by [25]. For spectral characterization, a dozen of the solar Fraunhofer lines were used to register spectral channels to a wavelength with an accuracy of ¡1 nm. During this process, the instrument is pointed at the Sun. The instrument records the spectrum and captures the characteristic dips at the Fraunhofer line positions. The measured positions of the Fraunhofer lines are then compared to their known absolute wavelengths. The instrument's wavelength assignment is corrected (e.g., by shifting or scaling the wavelength axis). The spectral resolution is assessed by evaluating how sharp or broad the lines appear in the measured spectrum.

The radiometric calibration was done at Radiometric Calibration Lab (RCL) and the Goddard Laser for Absolute Measurement of Radiance (GLAMR) facilities of NASA GSFC. RCL, the Radiometric Calibration Laboratory at NASA/GSFC, is a Class 10,000 clean room facility equipped with several NIST-traceable integrating sphere sources. In this study, we utilized a uniform spectral radiance light source from RCL known as Grande. Grande is a 101.6 cm diameter integrating sphere lined with Spectralon, featuring a 25.4 cm diameter output aperture and capable of producing nine distinct levels of light output. More detailed specifications can be found in [?]. GLAMR is a specialized spectral and radiometric calibration facility that employs a tunable laser to generate monochromatic, extended light sources for the precise calibration of hyperspectral instruments. It also has large integrating sphere sources with NIST-traceable radiometric calibration. For more information refer to https://glamr.gsfc.nasa.gov/ (last accessed 16 April 2025).

The ResPan-48 spectra were scaled by ±5% to account for potential errors for the reference SZA of 65.2° (on December 12th, 2023 in ??). The percentage difference between the model and the observation was found to be within 5% in the AOD retrieval for this reference date and SZA, as shown in fig. 24. Thereafter, the scaling factor was consistently applied to all AOD retrieval cases using ResPan-48.

.

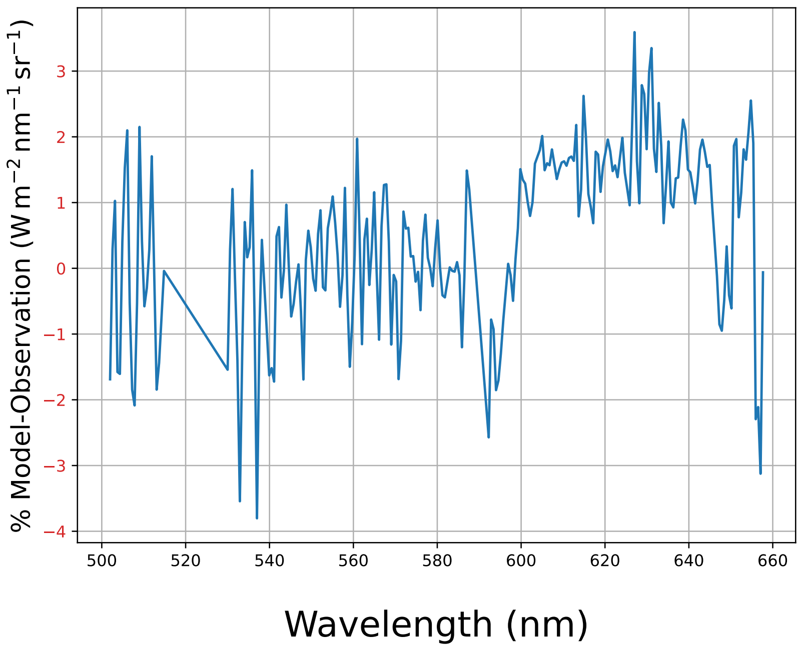

Figure 24: Percentage Difference between Model (DISORT) and observation (ResPan-48) for SZA 65.2° (reference point discussed in ??))

For the error analysis of the color ratio method discussed in (Figure 7 and Figure 11), the spectral ratio $R_{spectral}$ is given by:

$$R_{\text{spectral}} = \frac{I_{775}}{I_{450}},$$

where I_{775} is the intensity at the wavelength 775 nm, and I_{450} is the intensity at the wavelength 450 nm. The propagated uncertainty in R_{spectral} is:

$$\frac{\delta R_{\text{spectral}}}{R_{\text{spectral}}} = \sqrt{\left(\frac{\delta I_{775}}{I_{775}}\right)^2 + \left(\frac{\delta I_{450}}{I_{450}}\right)^2},$$

where $\delta R_{\text{spectral}}$ is the absolute uncertainty in the spectral ratio, δI_{775} is the uncertainty in the intensity at 775 nm, and δI_{450} is the uncertainty in the intensity at 450 nm. The absolute uncertainty, $\delta R_{\text{spectral}}$, can be written as:

$$\delta R_{\text{spectral}} = R_{\text{spectral}} \cdot \sqrt{\left(\frac{\delta I_{775}}{I_{775}}\right)^2 + \left(\frac{\delta I_{450}}{I_{450}}\right)^2}.$$

10 Appendix C

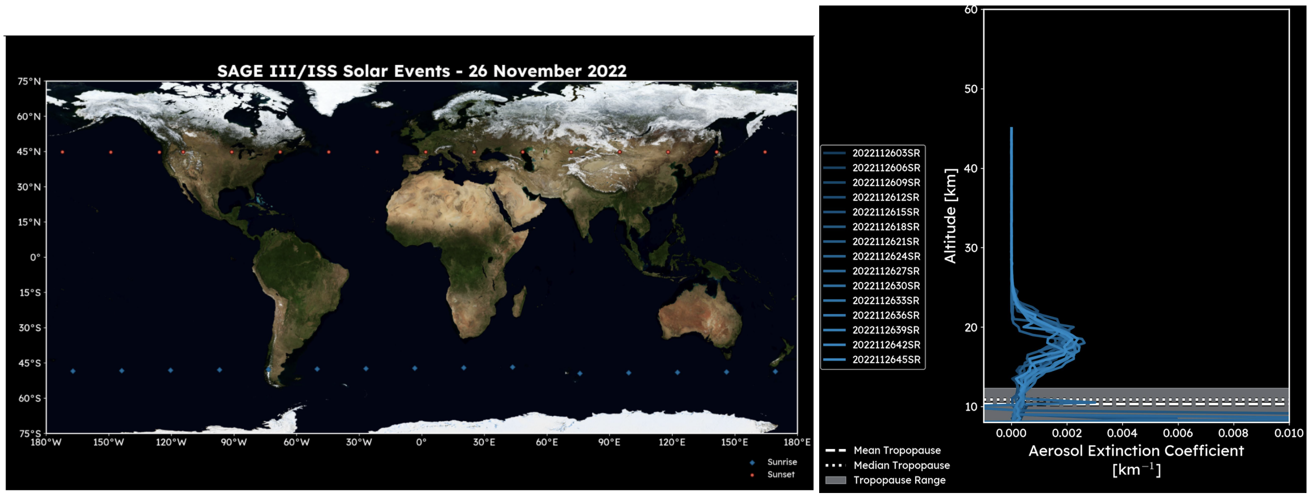

(a) Daily Event coverage map

(b) 1021 Aerosol Extinction coefficient

Figure 25: SAGE data for November 26, 2022, from Lauder, New Zealand.

11 Acknowledgments and Funding

The authors would like to acknowledge libRadtran, the AERONET team for the model and data, respectively, the GLAMR and Grande facilities at NASA GSFC for instrument calibrations, as well as Si-Chee Tsay, the PI of the ResPan spectroradiometer. The JPL Table Mountain lidar profiles used in this publication were obtained using support from the NASA Upper Atmosphere Research Program as part of the Network for the Detection of Atmospheric Composition Change (NDACC), and are available through the NDACC website www.ndacc.org. We thank Dr. Steve Davis for providing the 1050 nm twilight photometer aerosol profile from Brea, California. The MPLNET project is funded by the NASA Radiation Sciences Program and Earth Observing System. Lidar observation at Lauder is funded in part by the GOSAT (Greenhouse gases Observing SATellite) series project.

This research was funded by TSIS and Sun-Climate Research Supports to GSFC.

References

[1] Devang Mehta, Sabine Scandola, Curtis Kennedy, Christina Lummer, Maria Camila Rodriguez Gallo, Lauren E. Grubb, Maryalle Tan, Enrico Scarpella, and R. Glen Uhrig. Twilight length alters growth and flowering time in arabidopsis via ¡i¿lhy¡/i¿/¡i¿cca1¡/i¿. *Science Advances*, 10(26):eadl3199, 2024.

[2] Allen D. Riley. Power hours: The magic of twilight. `https://www.thefisherman.com/article/power-hours-the-magic-of-twilight/`, 2020. Accessed: 2024.

[3] Svetlana Rickel and Amatzia Genin. Twilight transitions in coral reef fish: the input of light-induced changes in foraging behaviour. *Animal Behaviour*, 70(1):133–144, 2005.

[4] Tom Bol. Can you photograph northern lights in nautical twilight? `https://www.tombolphoto.com/can-you-photograph-northern-lights-in-nautical-twilight/`, 2022. Accessed: 2024.

[5] HERBERT H. KIMBALL. Photometric measurements of daylight illumination on a horizontal surface at mount weather, va. *Monthly Weather Review*, 42(12):650 – 653, 1914.

[6] Arvid Ljunghall. The intensity of twilight and its connection with the density of the atmosphere. *Meddelanden fran Lunds Astronomiska Observatorium Serie II*, 125:5–171, January 1949.

[7] E. K. Bigg. The detection of atmospheric dust and temperature inversions by twilight scattering. *Journal of Atmospheric Sciences*, 13(3):262 – 268, 1956.

[8] E. K. Bigg. Atmospheric stratification revealed by twilight scattering. *Tellus*, 16(1):76–83, 1964.

[9] G. E. Shaw. Radiance and color of the sky at twilight - Perturbations caused by stratospheric haze. *Pure and Applied Geophysics*, 119(2):231–247, January 1981.

[10] Iuri Mateshvili, Giuli Mateshvili, and Nino Mateshvili. Measurement of the vertical aerosol distribution in the middle atmosphere by the twilight sounding method. *Journal of Aerosol Science*, 29(10):1189–1198, 1998.

[11] Nina Mateshvili and Frans JM Rietmeijer. Stratospheric dust loading from early 1981 to september 1985 based on the twilight sounding method and stratospheric dust collections. *Journal of volcanology and geothermal research*, 120(1-2):55–69, 2003.

[12] Nina Mateshvili, Didier Fussen, Filip Vanhellemont, Christine Bingen, Erkki Kyrölä, Iuri Mateshvili, and Giuli Mateshvili. Twilight sky brightness measurements as a useful tool for stratospheric aerosol investigations. *Journal of Geophysical Research: Atmospheres*, 110(D9), 2005.

[13] N Mateshvili, D Fussen, G Mateshvili, I Mateshvili, F Vanhellemont, E Kyrölä, S Tukiainen, J Kujanpää, C Bingen, C Robert, et al. Nabro volcano aerosol in the stratosphere over georgia, south caucasus from ground-based spectrometry of twilight sky brightness. *Atmospheric Measurement Techniques*, 6(10):2563–2576, 2013.

[14] Ellsworth G Dutton and John R Christy. Solar radiative forcing at selected locations and evidence for global lower tropospheric cooling following the eruptions of el chichón and pinatubo. *Geophysical research letters*, 19(23):2313–2316, 1992.

[15] Giovanni Pitari, Glauco Di Genova, Eva Mancini, Daniele Visioni, Ilaria Gandolfi, and Irene Cionni. Stratospheric aerosols from major volcanic eruptions: A composition-climate model study of the aerosol cloud dispersal and e-folding time. *Atmosphere*, 7:75, 05 2016.

[16] Michael Mills, A. Langford, T. O'Leary, K. Arpag, H. Miller, Michael Proffitt, R. Sanders, and Sule Solomon. On the relationship between stratospheric aerosols and nitrogen dioxide. *Geophysical Research Letters - GEOPHYS RES LETT*, 20:1187–1190, 06 1993.

[17] Arlin J Krueger. Sighting of el chichon sulfur dioxide clouds with the nimbus 7 total ozone mapping spectrometer. *Science*, 220(4604):1377–1379, 1983.

[18] G. S. Kent, U. O. Farrukh, P. H. Wang, and A. Deepak. Sage i and sam ii measurements of 1 μ m aerosol extinction in the free troposphere. *Journal of Applied Meteorology and Climatology*, 27(3):269–279, 1988.

[19] M. P. McCormick G. S. Kent and P.H. Wang. Validation of stratospheric aerosol and gas experiments i and ii satellite aerosol optical depth measurements using surface radiometer data. *Journal of Geophysical Research: Atmospheres*, 99(D5):10333–10339, 1994.

[20] E. Remsberg and G. Lingenfelser. Analysis of sage ii ozone of the middle and upper stratosphere for its response to a decadal-scale forcing. *Atmospheric Chemistry and Physics*, 10(23):11779–11790, 2010.

[21] Robert P Damadeo, Viktoria F Sofieva, Alexei Rozanov, and Larry W Thomason. An empirical characterization of the aerosol ångström exponent interpolation bias using sage iii/iss data. *Atmospheric Measurement Techniques Discussions*, 2023:1–13, 2023.

[22] Steven A Ackerman. Using the radiative temperature difference at 3.7 and 11 μm to tract dust outbreaks. *Remote Sensing of Environment*, 27(2):129–133, 1989.

[23] Xiaoyi Zhao, Debora Griffin, Vitali Fioletov, Chris McLinden, Jonathan Davies, Akira Ogyu, Sum Chi Lee, Alexandru Lupu, Michael D Moran, Alexander Cede, et al. Retrieval of total column and surface no 2 from pandora zenith-sky measurements. *Atmospheric Chemistry and Physics*, 19(16):10619–10642, 2019.

[24] Bernhard Mayer and Arve Kylling. The libradtran software package for radiative transfer calculations-description and examples of use. *Atmospheric Chemistry and Physics*, 5(7):1855–1877, 2005.

[25] Ukkyo Jeong, Si-Chee Tsay, N. Christina Hsu, David M. Giles, John W. Cooper, Jaehwa Lee, Robert J. Swap, Brent N. Holben, James J. Butler, Sheng-Hsiang Wang, Somporn Chantara, Hyunkee Hong, Donghee Kim, and Jhoon Kim. Simultaneous retrievals of biomass burning aerosols and trace gases from the ultraviolet to near-infrared over northern thailand during the 2019 pre-monsoon season. *Atmospheric Chemistry & Physics*, 22(18):11957–11986, September 2022.

[26] Sriperambudur Udaya Laxmi, Sonnati Chandralingam, Pullaiahgari Venkata Nagamani, Inaganti Veera Ganga Bhavani, Yerramsetti Umamaheswara Rao, et al. Importance of aerosol optical depth in the atmospheric correction of ocean colour remote sensing data. *Open Journal of Marine Science*, 7(01):100, 2017.

[27] Daniel Rosenfeld, Steven Sherwood, Robert Wood, and Leo Donner. Climate effects of aerosol-cloud interactions. *Science*, 343(6169):379–380, 2014.

[28] E. M Wilcox. Direct and semi-direct radiative forcing of smoke aerosols over clouds. *Atmospheric Chemistry and Physics*, 12(11):139–149, 2012.

[29] Arve Kylling, Sophie Vandenbussche, Virginie Capelle, Juan Cuesta, Lars Klüser, Luca Lelli, Thomas Popp, Kerstin Stebel, and Pepijn Veefkind. Comparison of dust-layer heights from active and passive satellite sensors. *Atmospheric Measurement Techniques*, 11(5):2911–2936, 2018.

[30] Rajendra K Pachauri, Myles R Allen, Vicente R Barros, John Broome, Wolfgang Cramer, Renate Christ, John A Church, Leon Clarke, Qin Dahe, Purnamita Dasgupta, et al. *Climate change 2014: synthesis report. Contribution of Working Groups I, II and III to the fifth assessment report of the Intergovernmental Panel on Climate Change*. Ipcc, 2014.

[31] Lena Katharina Jänicke, Rene Preusker, Nicole Docter, and Jürgen Fischer. Estimation of aerosol layer height from olci measurements in the o 2a-absorption band over oceans. *Remote Sensing*, 15(16):4080, 2023.

[32] JL Guerrero-Rascado, B Ruiz, and L Alados-Arboledas. Multi-spectral lidar characterization of the vertical structure of saharan dust aerosol over southern spain. *Atmospheric Environment*, 42(11):2668–2681, 2008.

[33] Iuri Mateshvili, Giuli Mateshvili, and Nino Mateshvili. Measurement of the vertical aerosol distribution in the middle atmosphere by the twilight sounding method. *Journal of aerosol science*, 29(10):1189–1198, 1998.

[34] EO Hulburt. Explanation of the brightness and color of the sky, particularly the twilight sky. *JOSA*, 43(2):113–118, 1953.

[35] C. Emde, R. Buras-Schnell, A. Kylling, B. Mayer, J. Gasteiger, U. Hamann, J. Kylling, B. Richter, C. Pause, T. Dowling, , and L. Bugliaro. The libRadtran software package for radiative transfer calculations (version 2.0.1). *Geosci. Model Dev.*, 9:1647–1672, 2016.

[36] C. Emde and B. Mayer. Simulation of solar radiation during a total eclipse: a challenge for radiative transfer. *Atmospheric Chemistry and Physics*, 7(9):2259–2270, 2007.

[37] C. A. Randles, A. M. da Silva, V. Buchard, P. R. Colarco, A. Darmenov, R. Govindaraju, A. Smirnov, B. Holben, R. Ferrare, J. Hair, Y. Shinozuka, and C. J. Flynn. The merra-2 aerosol reanalysis, 1980 onward. part i: System description and data assimilation evaluation. *Journal of Climate*, 30(17):6823 – 6850, 2017.

[38] Christos S Zerefos, VT Gerogiannis, Dimitris Balis, SC Zerefos, and Andreas Kazantzidis. Atmospheric effects of volcanic eruptions as seen by famous artists and depicted in their paintings. *Atmospheric Chemistry and Physics*, 7(15):4027–4042, 2007.

[39] Christian von Savigny, Anna Lange, Anne Hemkendreis, Christoph Hoffmann, and Alexei Rozanov. Is it possible to estimate aerosol optical depth from historic colour paintings? *Climate of the Past Discussions*, 2022:1–15, 2022.

[40] K.H. Lloyd. Calculation of the effective height of the earth's shadow. *Planetary and Space Science*, 16(8):1071–1073, 1968.

[41] Georgij V Rozenberg. *Twilight*. Springer, 1966.

[42] Stefano Corradini and Marco Cervino. Aerosol extinction coefficient profile retrieval in the oxygen a-band considering multiple scattering atmosphere. test case: Sciamachy nadir simulated measurements. *Journal of Quantitative Spectroscopy and Radiative Transfer*, 97(3):354–380, 2006.

[43] Alexander A Kokhanovsky and Vladimir V Rozanov. The determination of dust cloud altitudes from a satellite using hyperspectral measurements in the gaseous absorption band. *International Journal of Remote Sensing*, 31(10):2729–2744, 2010.

[44] Abram FJ Sanders, Johan F De Haan, and J Pepijn Veefkind. Retrieval of aerosol height from the oxygen a band with tropomi. *Proceedings of Advances in Atmospheric Science and Applications, Bruges, Belgium*, pages 18–22, 2012.

[45] S Sanghavi, JV Martonchik, J Landgraf, and U Platt. Retrieval of the optical depth and vertical distribution of particulate scatterers in the atmosphere using o 2 a-and b-band sciamachy observations over kanpur: a case study. *Atmospheric Measurement Techniques*, 5(5):1099–1119, 2012.

[46] Q Min, B Yin, S Li, J Berndt, L Harrison, E Joseph, M Duan, and P Kiedron. A high-resolution oxygen a-band spectrometer (habs) and its radiation closure. *Atmospheric Measurement Techniques*, 7(6):1711–1722, 2014.

[47] Lee Harrison and Qilong Min. Photon pathlength distributions from o2 a-band absorption. In *Proceedings of the International Radiation Symposium, August*, pages 19–24, 1996.

[48] AA Floutsi, MB Korras-Carraca, C Matsoukas, N Hatzianastassiou, and G Biskos. Climatology and trends of aerosol optical depth over the mediterranean basin during the last 12 years (2002–2014) based on collection 006 modis-aqua data. *Science of the Total Environment*, 551:292–303, 2016.

[49] O. M. Coddington, E. C. Richard, D. Harber, P. Pilewskie, T. N. Woods, M. Snow, K. Chance, X. Liu, and K. Sun. Version 2 of the tsis-1 hybrid solar reference spectrum and extension to the full spectrum. *Earth and Space Science*, 10(3):e2022EA002637, 2023. e2022EA002637 2022EA002637.

[50] B. Mayer. Radiative transfer in the cloudy atmosphere. *European Physical Journal Conferences*, 1:75–99, 2009.

[51] K. Stamnes, S.C. Tsay, W. Wiscombe, and K. Jayaweera. A numerically stable algorithm for discrete-ordinate-method radiative transfer in multiple scattering and emitting layered media. 27(12):2502–2509, 1988.

[52] Atmospheric Administration and United States Committee on Extension to the Standard Atmosphere. *US Standard Atmosphere, 1976*. National Oceanic and Amospheric [sic] Administration, 1976.

[53] Jay Herman, Alexander Cede, Elena Spinei, George Mount, Maria Tzortziou, and Nader Abuhassan. No2 column amounts from ground-based pandora and mfdoas spectrometers using the direct-sun doas technique: Intercomparisons and application to omi validation. *Journal of Geophysical Research: Atmospheres*, 114(D13), 2009.

[54] J. Herman, R. Evans, A. Cede, N. Abuhassan, I. Petropavlovskikh, and G. McConville. Comparison of ozone retrievals from the pandora spectrometer system and dobson spectrophotometer in boulder, colorado. *Atmospheric Measurement Techniques*, 8(8):3407–3418, 2015.

[55] B.N. Holben, T.F. Eck, I. Slutsker, D. Tanré, J.P. Buis, A. Setzer, E. Vermote, J.A. Reagan, Y.J. Kaufman, T. Nakajima, F. Lavenu, I. Jankowiak, and A. Smirnov. Aeronet—a federated instrument network and data archive for aerosol characterization. *Remote Sensing of Environment*, 66(1):1–16, 1998.

[56] A. Sinyuk, B. N. Holben, T. F. Eck, D. M. Giles, I. Slutsker, S. Korkin, J. S. Schafer, A. Smirnov, M. Sorokin, and A. Lyapustin. The aeronet version 3 aerosol retrieval algorithm, associated uncertainties and comparisons to version 2. *Atmospheric Measurement Techniques*, 13(6):3375–3411, 2020.

[57] GES DISC, 2016, Giovanni, howpublished = `http://giovanni.gsfc.nasa.gov/`, note = Accessed: 2024.

[58] Forrest M. Mims III. An inexpensive and stable led sun photometer for measuring the water vapor column over south texas from 1990 to 2001. *Geophysical Research Letters*, 29(13):20–1–20–4, 2002.

[59] Forrest M. Mims III. Build a twilight photometer to detect stratospheric particles. *Build a Twilight Photometer to Detect Stratospheric Particles - Make: (makezine.com)*, pages 84–85, 2015.

[60] Thierry Leblanc. Lidar 101: Introduction to the jpl lidars. `https://tmf.jpl.nasa.gov/tmf-lidar/instruments/instruments_intro.htm/`, 2024. Accessed: 2024.

[61] Wolfgang Steinbrecht and Thierry Leblanc. Lidars in the network for detection of atmospheric composition change (ndacc) and the tropospheric ozone lidar network (tolnet). In *Handbook of Air Quality and Climate Change*, pages 1–24. Springer, 2022.

[62] T Leblanc, IS McDermid, and TD Walsh. Ground-based water vapor raman lidar measurements up to the upper troposphere and lower stratosphere for long-term monitoring. *Atmospheric Measurement Techniques*, 5(1):17–36, 2012.

[63] Ellsworth J Welton, James R Campbell, James D Spinhirne, and V Stanley Scott III. Global monitoring of clouds and aerosols using a network of micropulse lidar systems. In *Lidar remote sensing for industry and environment monitoring*, volume 4153, pages 151–158. SPIE, 2001.

[64] Ellsworth J Welton, Sebastian A Stewart, Jasper R Lewis, Larry R Belcher, James R Campbell, and Simone Lolli. Status of the nasa micro pulse lidar network (mplnet): overview of the network and future plans, new version 3 data products, and the polarized mpl. In *EPJ Web of Conferences*, volume 176, page 09003. EDP Sciences, 2018.

[65] A Smirnov, BN Holben, TF Eck, O Dubovik, and I Slutsker. Cloud-screening and quality control algorithms for the aeronet database. *Remote sensing of environment*, 73(3):337–349, 2000.

[66] G. G. Bennett. The calculation of astronomical refraction in marine navigation. *Journal of Navigation*, 35:255–259, January 1982.

[67] T Sakai, O Uchino, T Nagai, B Liley, I Morino, and T Fujimoto. Long-term variation of stratospheric aerosols observed with lidars over tsukuba, japan, from 1982 and lauder, new zealand, from 1992 to 2015. *Journal of Geophysical Research: Atmospheres*, 121(17):10–283, 2016.

[68] Tetsu Sakai, Takashi Shibata, and Yasunobu Iwasaka. Relative humidity, backscattering ratio and depolarization ratio as derived from raman lidar observations. *Journal of the Meteorological Society of Japan. Ser. II*, 75(6):1179–1185, 1997.

[69] S. P. Parajuli, G. L. Stenchikov, A. Ukhov, I. Shevchenko, O. Dubovik, and A. Lopatin. Aerosol vertical distribution and interactions with land/sea breezes over the eastern coast of the red sea from lidar data and high-resolution wrf-chem simulations. *Atmospheric Chemistry and Physics*, 20(24):16089–16116, 2020.